Thruster modeling for small unmanned aerial vehicles with coaxial-rotors

Tsvi Tsadok

Master of Engineering

Department of Mechanical Engineering

McGill University

Montreal, Quebec

Friday 1st August, 2014

A thesis submitted to McGill University in partial fulfilment
of the requirements of the degree of Master of Engineering

DEDICATION

To Meytal, my beautiful wife.

ACKNOWLEDGMENTS

I would like to express my sincere gratitude to my supervisor, prof. Meyer Nahon, for his knowledge, attention to details, critiques, guidance and patience, along with his warm personality that enabled me to complete this thesis. This work could have never been accomplished without his guidance. Additional thanks is addressed to prof. Inna Sharf who believed in me and agreed to join me to her research group and let me lead the coaxial-rotor thruster modeling. I would also like to thank all my previous and current teammates in the Aerospace Mechatronics Lab at McGill university who assisted me when needed. I would like to thank Mr. Matt Michini who brought me up to speed with the work he has accomplished with thruster modeling and the build of our test-stand, which allowed me to have an easy start for this study. Special thanks deserves Mr. Waqas Khan who, with his wide knowledge in aerodynamics, helped me overcome some of the obstacles I encountered during this work. Additional thanks is addressed to Mr. Eitan Bulka who assisted me with the various topics towards the final steps of this work. For the excellent French translation of the abstract I would like to thank Mr. Louis-Martin Deslandes. I am deeply grateful for the support I received from my friends and family and to my ”Le Plateau family” in specific. Lastly, this thesis could have never been completed without the support of my best friend and life companion, my wife, Meytal, who advised me in almost every aspect of this work. Her love, warmth and wisdom allowed me to keep going even in the hardest steps along the way.

ABSTRACT

This thesis work uses the blade element momentum theory (BEMT) to model coaxial-rotor thrusters of small unmanned aerial vehicles (UAVs) in order to predict the thrust produced with this rotor configuration. In order to use the developed BEMT model, the geometrical and aerodynamics characteristics of the rotor are obtained by slicing the propeller blade into several sections. This process is described in the thesis and enables the extraction of the chord, pitch angle and airfoil coordinates. With the obtained airfoil coordinates, the zero-lift angle and drag coefficient are simulated using MIT's XFOIL software. Experiments were then conducted to validate the simulation results. The construction of the test-stand for measuring thrust and torque of single and coaxial-rotor configurations of small UAV is described. In general, good agreement was found between simulations and experiments. It is shown that inclusion of swirl velocity and removing the assumption of small angles in the BEMT model do not significantly improve the accuracy of thrust prediction for the hover case of single rotors. Thus, for simplicity, the model for the coaxial-rotor assumes small angles and ignores the swirl. Following the validation of the BEMT model to predict thrust for the hover case, axial flight simulation is also validated by comparison to wind tunnel measurements, available on-line Finally, ground effect is investigated experimentally for the single-rotor. It is shown that the use of Cheeseman and Bennett formula for predicting the thrust increase at constant power can also be used to predict the thrust increase at constant rotational speeds of the rotor.

ABRÉGÉ

Dans cette thèse, la théorie de l'inertie de l'élément de pale (TIEP) est utilisée pour modéliser le rotor-propulseur de petits aéronefs téléguidés dans le but de prédire la poussée produite par cette configuration de rotor. Afin de pouvoir utiliser le modèle TIEP, les propriétés géométriques et aérodynamiques du rotor sont obtenues en tranchant les pales de propulsion en plusieurs coupes. La méthode décrite dans cette thèse permet d'extraire la corde, l'angle de pas et les coordonnées de surface portante. Ces coordonnées permettent de simuler l'incidence de portance nulle et le coefficient de trainée à l'aide du logiciel XFOIL du MIT. Des expériences ont été menées pour valider les résultats de simulation. La construction du banc d'essai pour mesurer la poussée et le couple de rotors simples et coaxiaux d'aéronefs téléguidés est décrite. En général, les résultats de simulations concordent bien avec les expériences. Il est démontré que l'inclusion d'une vitesse de tourbillon et l'omission de l'hypothèse des petits angles du modèle TIEP n'améliorent pas de manière significative la justesse des prédictions de poussée dans le cas de vols stationnaires de rotors simples. Pour cette raison, le modèle pour un rotor-coaxial considère de petits angles et ignore le tourbillon. Suite à la validation du modèle TIEP pour prédire la poussée de vols stationnaires, des vols axiaux sont simulés et aussi validés en comparaison avec des mesures en soufflerie, disponibles en ligne. Finalement, l'effet de sol est étudié expérimentalement pour le rotor simple. Il est démontré que l'utilisation de la formule de Cheeseman et Bennet, utilisée pour prédire l'augmentation de poussée à puissance constante, peut aussi être utilisée pour prédire l'augmentation de poussée à vitesse constante de rotation du rotor.

TABLE OF CONTENTS

LIST OF TABLES

LIST OF FIGURES

NOMENCLATURE

α_0	Zero-lift angle
$\square_l$	Subscript lower rotor
$\square_u$	Subscript upper rotor
θ	Pitch angle
A	Rotor disk area
C_p	Power coefficient definition from UIUC, $= P/\left(\rho n^3 D^5\right)$
C_t	Thrust coefficient definition from UIUC, $= T/\left(\rho n^2 D^4\right)$
r	Non-dimensional local radius
z	Maximum camber
α	Angle of attack, $= \theta + \alpha_0 - \phi$
Ω	Angular velocity
ϕ	Inflow angle (induced angle of attack)
ρ	Air density
σ	Rotor local solidity, $N_b c/2\pi y$
A_c	Contracted slipstream wake area
c	Chord line length
C_P	Rotor power coefficient, $= P/\left(\rho A \Omega^3 R^3\right)$
C_T	Rotor thrust coefficient, $= T/\left(\rho A \Omega^2 R^2\right)$
$C_{l,\alpha}$	Lift curve slope

dD	Drag force
dF_R	Resultant force
dL	Lift force
dP	Power
dQ	Torque
dT	Thrust force
n	Propeller rotational speed, rev/s
N_b	Number of blades
P_{IGE}	Power in ground effect
P_{OGE}	Power out of ground effect
R	Blade radius
T_{IGE}	Thrust in ground effect
T_{OGE}	Thrust out of ground effect
u_i	Induced swirl velocity
V	Inflow velocity
V_∞	Climbing velocity
v_i	Induced inflow (axial) velocity
V_P	Perpendicular velocity
V_T	Tangential velocity
y	Local blade radius
Z	Height above the ground

ABBREVIATIONS

APC Advanced Precision Composites

BET Blade Element Theory

BEMT Blade Element Momentum Theory

CFD Computational Fluid Dynamics

DRDC Defence Research and Development Canada

ESC Electronic Speed Control

IGE In Ground Effect

Inc. Incorporation

OGE Out of Ground Effect

UAV Unmanned Aerial Vehicle

UIUC University of Illinois at Urbana-Champaign

Chapter 1
Introduction

Small unmanned aerial vehicles (UAV) are gaining popularity and are being used in both military and civil operations. Among these usages are surveillance, search & rescue, geographical mapping, real-estate marketing, television commercials, sport filming and others. Small UAVs have many different forms, with one of the most common being the helicopter UAV. There are several different possible rotor configurations, including: (a) the conventional helicopter, with a single main rotor and an anti-torque tail rotor; (b) the tandem rotor, with two rotors operating in parallel on the same or different planes (but not on the same axis); (c) the coaxial-rotor, with two counter-rotating rotors operating on the same axis; and (d) the quad-rotor, with four rotors equally spaced from each other. See Figs. 1–1a to 1–1d.

Another type of small helicopter UAV consists of an airframe with four coaxial-rotors in a quad-rotor configuration. In this configuration, each rotor pair can operate in a torque-balanced condition. This arrangement provides greater flexibility in control, due to the presence of eight, rather than four control inputs. Another advantage of the coaxial-rotor configuration (not limited only to the coaxial-rotor in quad arrangement) is the ability to carry heavier payload for the same UAV size, due to the larger thrust capacity of coaxial-rotors.

However, it should be noted that, due to the flow interaction between the two rotors, a coaxial-rotor produces less thrust than the sum of thrust produced by two single rotors.

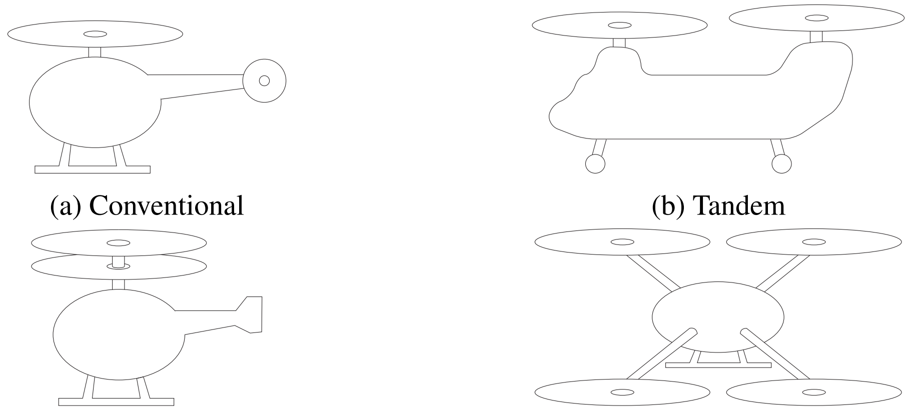

(a) Conventional (b) Tandem

(c) Coaxial (d) Quad

Figure 1–1: Different helicopter configurations

Leishman[3] has analytically showed that the coaxial-rotor requires approximately 22% more power for producing the same thrust produced by two single rotors separately. Similarly, experimental results[4] of comparison between thrusts produced in coaxial-rotor configuration and in combined two single-rotor configuration have shown an average of 23% reduction in produced thrust.

1.1 Draganflyer X8

The Draganflyer X8 (hereby referred as ”X8”) is a small helicopter UAV with coaxial-rotors in a quad configuration, developed by Draganfly Innovations Inc., shown in Fig. 1–2. The vehicle consists of a central platform with four molded carbon fiber folding arms that snap into place for assembly. A motor pod containing two motors is located at the end of each arm. Within each pod are two motors that spin counter-rotating fixed pitch molded carbon fiber rotor blades of different diameters (with upper radius $R_u =$ 203.2mm and lower radius $R_l =$ 190.5mm) for a total of eight rotors (i.e. four coaxial-rotors). The four arms are equally spaced with motors located at radius of 331mm from

Figure 1–2: Draganflyer X8

the center of the platform, which leads to upper and lower rotor clearance (i.e. minimum distance between rotors' tips) of 64mm and 85mm, respectively. The distance between the upper and the lower rotors (i.e. vertical rotor-spacing) is 100mm. The vehicle is equipped with lightweight carbon fiber skid-type landing gear, and is powered by a 14.4V lithium polymer battery with capacity of 5400mAh.

The X8 is equipped with several sensors to enable varying degrees of autonomy: an inertial measurement unit (IMU), a 3-axis magnetometer, a barometric pressure sensor, and a global positioning system (GPS) receiver. The aircraft's autopilot allows the operator to select the desired level of autonomy: manual throttle, altitude hold, or position hold. In manual throttle mode, the aircraft uses the IMU and magnetometer to maintain level flight and a selected heading, and the operator controls all other flight inputs, including height, via throttle. In altitude hold mode, the aircraft uses the pressure sensor to maintain an altitude set-point, while the position hold mode can be used to maintain a given 3D position using a combination of the pressure sensor and the GPS receiver.

The total size of the vehicle is 870 by 870 by 320 millimeters and is lightweight, weighing only 1700g and has a relatively large payload capability of 1000g.

1.2 Motivation and Objectives

A project funded by the Defence Research and Development Canada in Suffield, Alberta (DRDC-Suffield) is being conducted by researchers at McGill university. The overall purpose of the project is to improve the X8's autonomy. Among the objectives of this project are autonomy taking off, flying a certain path and landing.

In order to design autonomous controllers for the X8, a simulator is needed. For this purpose, it is important to have a good knowledge of the thrust produced for a given set of two angular velocities (one per rotor) of each coaxial-rotor pair. Beyond experimental quantification of thrust, it is also be useful to have models that can predict the generation of thrust for given rotor speeds.

Validation of the model is vital for assuring its accuracy. For that, a test-stand needs to be constructed for measuring the produced thrust and torque of the coaxial-rotor for a given set of rotational speeds. This will enable a comparison between the predicted thrust of the model and the measurements.

Since the X8 rotor blades are custom made out of expensive molded carbon fiber (approximately $200 for each rotor), evaluating some conventional low cost alternative rotors is considered. Performance measurements will be conducted, with the test-stand, for these alternative rotor blades. Comparing these measurements with the X8 performance experimental data will allow us evaluating the alternatives and find a rotor with similar or better efficiency, i.e. less power consumption, represented by smaller torque, for similar produced thrust

Since one of the main goals of the DRDC project is to achieve autonomy during take-off and landing, the ground effect, which reduces the amount of thrust required for hover near the ground, is also investigated here.

1.3 Literature Survey

One of the earliest appearances of an analysis of propellers, can be found at the end of the 19th century, when Rankine[5] studied marine propulsion and developed the momentum theory. This theory was further developed by W. Froude[6] and R. E. Froude[7] to develop, what we call today, Rankine-Froude axial momentum theory. In this theory, using a 1-D analysis, the propeller is modeled as an ideal actuator disk with the assumption that the thrust loading and flow velocity are uniform over the disk. This theory was later generalized by Glauert[8] for a propeller acting in air, considering the condition of its operation. The main drawback of momentum theory is that it ignores the shape of the propeller (i.e. its aerodynamic characteristics), which obviously has a large impact on its behaviour and performance.

A more sophisticated aerodynamic propellers analysis is the 2-D blade element theory (BET) which was first introduced in a crude form by Froude[6]. However, its main development is referred to the work of Drzewiecki[9][10]. In this theory, each propeller blade is divided into a large number of elements along its radius where each element is represented as a 2-D airfoil with the assumption that there is no mutual effect between adjacent blade elements.

In the mid 20th century, Gustafson and Gessow[11] suggested combining the two theories, developing blade element momentum theory (BEMT) for hovering rotors. The BEMT enables estimation of the inflow distribution along the blade after equating the lift calculated by the momentum theory with the lift from circulation theory used in the BET.

In the 1950's the hovering-performance theory by Gessow[12][1], developed for the hovering single-rotor, was adapted by Harrington[14] for the coaxial-rotor, by treating the coaxial-rotor as a four blades single-rotor but with the same solidity. In order to validate his theory, Harrington and Dingeldein[15] performed some measurements for a coaxial-rotor and also obtained a previously measured coaxial-rotor, naming the Harrington-rotor-1 and Harrington-rotor-2 respectively. To better understand the behaviour of a coaxial-rotor, Harrington and Dingeldein also performed measurements for a single rotor using the same propellers. Although the theoretical thrust performance prediction for the single-rotor had a very good agreement with the measurements, the prediction for the coaxial-rotor was, however, less accurate with approximately 5% over-prediction of required power for the same thrust[14]. More details about Harrington and other coaxial-rotor studies can be found in the comprehensive survey of theoretical and experimental coaxial-rotor research, which was performed by Coleman[16] in 1997.

As stated above, simple but reasonably good mathematical models have previously been developed for prediction of thrust in single rotor helicopters, but few models have been developed for thrust prediction of coaxial-rotors. Leishman has extensively studied

[1] The hovering-performance theory is a simplification of the airscrew strip theory developed by Lock[13]

the design, performance and behaviour of coaxial-rotors and has published several papers on the subject[17][3][18][19][20]. In his text book, "*Principles of Helicopter Aerodynamics*"[1], Leishman details a simple but thorough development of a BEMT model for the single rotor. In addition he shows a coaxial-rotor model using only the simple momentum theory, however this model over-pessimistically predicts the thrust vs. power. Later, Leishman and Ananthan[18] developed a more sophisticated mathematical model, based on BEMT, to predict the thrust and power of a coaxial-rotor in full size rotors, such as the Harrington rotor 1[14]. However, full size coaxial-rotors are usually operated with the upper and lower rotors spinning at equal and opposite speeds, and with automated and controlled pitch that changes during operation (i.e. collective pitch) to maintain a torque-balanced condition. By contrast, small UAV rotors (twisted or not) typically have fixed pitch blade, and the rotation speed of the two rotors is not equal, and can vary substantially during operation. Therefore, Leishman and Ananthan's model cannot be used directly for such UAVs. In this study we aim to adapt the BEMT model for a coaxial propeller pair, which is not restricted to torque-balanced rotors with constant and equal speed.

An analytical approach, based on the BEMT, for analyzing the coaxial-rotor performance was also presented by Yana and Rand[21]. This analysis does not limit the upper and lower rotors to have the same diameter, rotational speed nor number of blades. However, this model assumes that not only the lower rotor takes into account the inflow velocity of the upper rotor, but also the upper rotor takes into account the inflow velocity from the lower rotor as an "equivalent climbing speed". However, the assumption that the upper rotor is affected by the lower rotor, complicates the solution. Moreover, Leishman has already shown that assuming the upper rotor is not affected, is sufficient.

Another method for predicting helicopter performance is the vortex theory, which is an extension of Pranstl's lifting-line theory. This theory uses the concept of circulation and the Kutta-Joukowski theorem. This method is a 3-D analysis, which makes it more sophisticated than the 2-D BEMT analysis. Bagai and Leishman[17] performed a free-wake vortex analysis of a coaxial-rotor which was later used by Syal[22] for optimizing coaxial-rotor systems. The vortex theory advantage over the BEMT is mainly for solving rotors with high thrust settings, which is not the case in our current study.

The most advanced method for analyzing helicopter performance to date is the computational fluid dynamics (CFD), which solves and analyzes fluid flows problems using numerical methods and algorithms. Lakshminarayan[23] used a compressible Reynolds Averaged Navier Stokes (RANS) solver to investigate the aerodynamics of a micro-scaled coaxial-rotor configuration in hover. In his paper, Lakshminarayan showed that the overall performance is well predicted for a range of RPMs and rotor spacing. Unfortunately, CFD softwares requires extremely high computational resources, which can take days and weeks in order to solve a specific coaxial-rotor. Moreover, CFD method requires generation of grids, which is an entire challenge on its own.

Considering the pros and cons of the above mentioned methods, the BEMT method, developed by Leishman and Ananthan[3], is the most suitable for our case, even though it requires some modifications.

1.4 Thesis Organization

This thesis is divided into five chapters. The first chapter includes an introduction to this study. The second chapter details the physics-based mathematical development of the thruster model for a single rotor, using the BEMT, and its validity. It also describes the custom made test-stand for measuring the thrust produced by a propeller. The third chapter details an evolvement of the BEMT model developed in chapter 2 in order to be suitable for a coaxial-rotor. The fourth chapter discusses the ground effect. The fifth and last chapter concludes the work in the thesis and recommends few suggestions for future work.

Chapter 2
Single Rotor Modeling and Experiments

2.1 BEMT Developed for the Single Rotor

The blade element momentum theory enables estimations of the inflow distributed along a rotor blade by equating the lift obtained from the BET and from the momentum theory.

In this chapter we will detail the development of the BEMT model and the methods for obtaining the geometric and aerodynamic characteristics of a rotor to be used in the model. Then, using experimental data obtained with a custom-made test-stand measurements and from external sources, we will validate the model for both the hover and the axial flight cases.

2.1.1 BEMT assumptions

The development of the BEMT model for a single rotor requires a few assumptions for simplification. First, we assume that all angles remain small. Second, we assume that adjacent rotor annuli have no mutual effect on each other. Third, we assume that the lift curve slope is constant. Finally we assume that swirl can be neglected ($u_i = 0$), which was previously proven to be a reasonable assumption[1]. We also assume that the downwash velocity has a constant momentum value given by eq. 2.23.

2.1.2 Blade element theory

In blade element theory, each section of the blade is treated as an infinite wing, represented as an airfoil. An example of one section, along with the forces acting on it and the flow velocities around it, is shown in Fig. 2–1. In this diagram, we can see the inflow

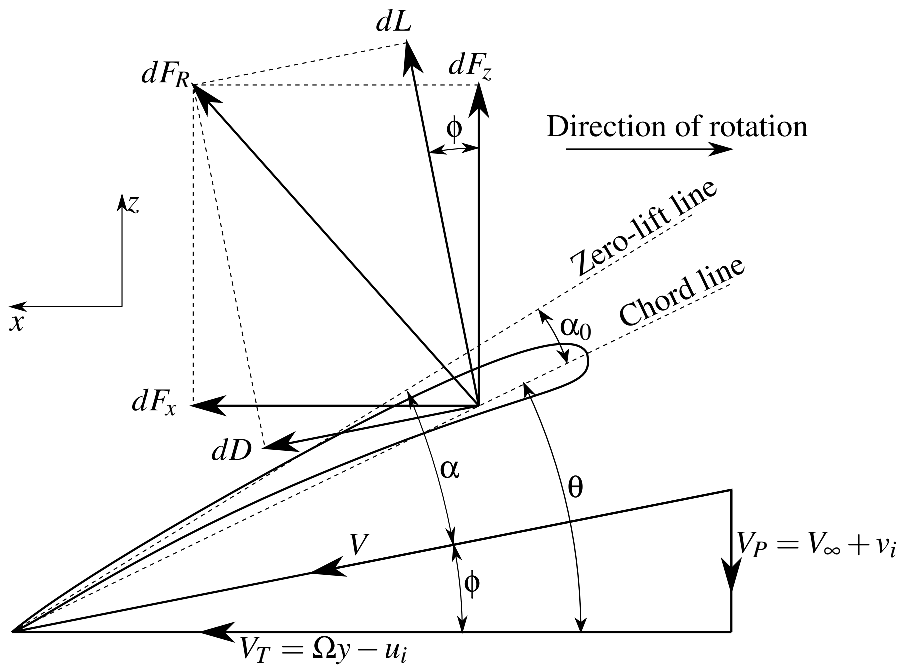

Figure 2–1: Airfoil diagram

velocity, V, which is the resultant of the perpendicular and tangential velocities, V_P and V_T respectively. The inflow angle, ϕ, determined by the angle between the inflow and the direction of rotation, is obtained by the inverse tangent of the relation V_P/V_T. The pitch angle, θ, is determined by the geometric shape of the rotor blade and is measured between the chord line and the direction of rotation. The zero-lift angle, exists only for cambered airfoils and is noted by α_0, is the angle between the zero-lift line and the chord line. The angle of attack, α, is simply the angle between the inflow velocity and the zero-lift line, which can be calculated by $\alpha = (\theta - \phi + \alpha_0)$. The elemental lift and drag forces, represented by dL and dD, acting on the blade section, are perpendicular and parallel to the inflow velocity, respectively. These forces are used to calculate the vertical and horizontal, dF_z and dF_x, forces. The direction of rotation is given in the diagram.

We will now analyze the forces acting on the blade element. Those forces, summed over all elements, will allow us to determine the thrust and torque produced by the propeller.

From circulation theory, the lift and drag forces produced by the blade element are

$$dL = \frac{1}{2}\rho V^2 c C_l dy \tag{2.1}$$

$$dD = \frac{1}{2}\rho V^2 c C_d dy. \tag{2.2}$$

From Fig. 2–1, the lift and drag can be rewritten as forces in the x and z directions:

$$dF_z = dL\cos\phi - dD\sin\phi \tag{2.3}$$

$$dF_x = dL\sin\phi + dD\cos\phi. \tag{2.4}$$

where ϕ is the inflow angle. Those forces can, in turn, be used to express the thrust, torque and power acting on each annulus as

$$dT = N_b\left(dL\cos\phi - dD\sin\phi\right) \tag{2.5}$$

$$dQ = N_b\left(dL\sin\phi + dD\cos\phi\right)y \tag{2.6}$$

$$dP = N_b\left(dL\sin\phi + dD\cos\phi\right)\Omega y \tag{2.7}$$

where N_b is the number of blades and y is the local radius (i.e. radial location of the element).

Assuming the inflow angle, ϕ, is small and because the drag force is at least one order of magnitude smaller than the lift, which means $dD \cdot \phi \ll dL$, we can write

$$dT = N_b dL \tag{2.8}$$

$$dQ = N_b \left(dL\phi + dD\right) y \tag{2.9}$$

$$dP = N_b \left(dL\phi + dD\right) \Omega y. \tag{2.10}$$

Assuming $V_T \gg V_P \Rightarrow V \approx V_T$ (as a result of small angles) and using eq. 2.1 and eq. 2.8 we can write the elemental thrust as

$$dT = \frac{1}{2} N_b \rho \left(\Omega y\right)^2 c C_l dy. \tag{2.11}$$

Defining the non-dimensional values

$$\lambda_\infty = \frac{V_\infty}{\Omega R}, \tag{2.12}$$

$$\lambda_i = \frac{v_i}{\Omega R}, \tag{2.13}$$

$$r = \frac{y}{R} \tag{2.14}$$

and

$$\lambda = \lambda_\infty + \lambda_i. \tag{2.15}$$

Hence, assuming small inflow angle, which translates to $\phi \approx \frac{V_\infty + v_i}{\Omega y}$, the inflow angle can be written as $\phi = \frac{\lambda}{r}$.

Now, let us define the non-dimensional thrust, power and torque coefficients for the blade element by

$$dC_T = \frac{dT}{\rho A (\Omega R)^2} \tag{2.16}$$

$$dC_P = \frac{dP}{\rho A (\Omega R)^3} \tag{2.17}$$

$$dC_Q = \frac{dQ}{\rho A (\Omega R)^2 R}. \tag{2.18}$$

With the relationship between the thrust and the lift from eq. 2.11 and the definition of the thrust coefficient from eq. 2.16 we can write the thrust coefficient as

$$dC_T = \frac{\frac{1}{2} N_b \rho (\Omega y)^2 c C_l dy}{\rho \pi R^2 (\Omega R)^2} = \sigma C_l r^3 dr, \tag{2.19}$$

where $\sigma = \frac{N_b c}{2\pi y}$ is defined as the *local* solidity. It is important to note that, in these equations, c represents the *local* chord.

If we now assume that the lift curve slope, $C_{l,\alpha}$, is constant, then the lift coefficient can be written as $C_l = C_{l,\alpha}(\theta + \alpha_0 - \phi)$ and we can write the elemental thrust coefficient as

$$\begin{aligned} dC_T &= \sigma C_{l,\alpha} (\theta + \alpha_0 - \phi) r^3 dr \\ &= \sigma C_{l,\alpha} ((\theta + \alpha_0) r - \lambda) r^2 dr, \end{aligned} \tag{2.20}$$

where θ is the pitch angle, α_0 is the zero-lift angle due to camber of the airfoil and ϕ is the inflow angle.

Similarly, using eqs. 2.1, 2.2, 2.9 and 2.17 we can find the power and torque coefficients

$$
\begin{aligned}
dC_P \equiv dC_Q &= \frac{\frac{1}{2} N_b \rho \left(\Omega y\right)^3 c \left(C_l \phi + C_d\right) dy}{\rho \pi R^2 \left(\Omega R\right)^3} \\
&= \phi r \sigma C_l r^3 dr + \sigma C_d r^4 dr \\
&= \lambda dC_T + \sigma C_d r^4 dr, \qquad (2.21)
\end{aligned}
$$

where λdC_T represents the induced power and $\sigma C_d r^4 dr$ represents the profile power.

2.1.3 Momentum theory

The mass flow rate of air through an annulus of the propeller disk can be written as

$$
\begin{aligned}
d\dot{m} &= \rho \left(V_\infty + v_i\right) dA \\
&= \rho \left(V_\infty + v_i\right) 2\pi y \, dy. \qquad (2.22)
\end{aligned}
$$

Momentum theory can be used to show that the change of speed of the air, from far upstream to far downstream of the propeller, is twice the induced velocity at the propeller, v_i. The resulting change of momentum of the air is therefore $2v_i \, d\dot{m}$, which can be expanded as

$$
dT = 2\rho \left(V_\infty + v_i\right) v_i 2\pi y \, dy. \qquad (2.23)
$$

Using eq. 2.23, and with the thrust coefficient definition from eq. 2.16 we can write

$$
\begin{aligned}
dC_T &= \frac{dT}{\rho A (\Omega R)^2} \\
&= \frac{4\pi\rho (V_\infty + v_i) v_i y \, dy}{\rho\pi R^4 \Omega^2} \\
&= 4 (\lambda_\infty + \lambda_i) \lambda_i r \, dr
\end{aligned}
\tag{2.24}
$$

Now, rearranging eq. 2.15 to $\lambda_i = \lambda - \lambda_\infty$ leads to

$$
\begin{aligned}
dC_T &= 4 (\lambda_\infty + \lambda - \lambda_\infty)(\lambda - \lambda_\infty) r \, dr \\
&= 4\lambda (\lambda - \lambda_\infty) r \, dr.
\end{aligned}
\tag{2.25}
$$

The flow around the tip of the propeller blade is adversely affected by 3D effects. This can be accounted for using Prandtl's tip-loss factor[24], F, which leads to

$$dC_T = 4F\lambda (\lambda - \lambda_\infty) r \, dr \tag{2.26}$$

where

$$F = \left(\frac{2}{\pi}\right) \cos^{-1} (\exp(-f)) \tag{2.27}$$

and f is given in terms of the number of blades and the non-dimensional radial location of the blade element, r, by

$$f = \frac{N_b}{2} \left(\frac{1-r}{r\phi}\right). \tag{2.28}$$

Combining eq. 2.20 from the BET with eq. 2.26 from the momentum theory we have

$$\sigma C_{l,\alpha} ((\theta + \alpha_0) r - \lambda) r = 4F\lambda (\lambda - \lambda_\infty) \tag{2.29}$$

and after rearrangement

$$\lambda^2 + \left(\frac{\sigma C_{l,\alpha}}{4F} r - \lambda_\infty\right)\lambda - \frac{\sigma C_{l,\alpha}}{4F}(\theta + \alpha_0) r^2 = 0. \tag{2.30}$$

The solution to this quadratic equation is given by

$$\lambda = \sqrt{\left(\frac{\sigma C_{l,\alpha}}{8F} r - \frac{\lambda_\infty}{2}\right)^2 + \frac{\sigma C_{l,\alpha}}{4F}(\theta + \alpha_0) r^2} - \left(\frac{\sigma C_{l,\alpha}}{8F} r - \frac{\lambda_\infty}{2}\right). \tag{2.31}$$

Because F, the tip loss correction factor, is a function of λ this equation must be solved iteratively by first calculating λ using $F = 1$. Once a solution is formed for λ, a new F is calculated using eq. 2.27 and the solution is repeated until it converges.

The calculated inflow value is then used to calculate the elemental thrust and power coefficients using eqs. 2.20 and 2.21 respectively. The elemental thrust and power coefficients are integrated along the rotor's radius to find the thrust and power coefficients, C_T and C_P for the rotor.

While the above analysis is accurate in many situations, it does make a few assumptions, including no stall, no swirl, and small angles. We are now interested to relax these assumptions, to see how this affects the analysis.

2.1.4 Stall

The preceding analysis presumes that $C_l = C_{l,\alpha}(\theta + \alpha_0 - \phi)$, which implies that lift increases monotonically with angle of attack, and the blades never stalls. In order to achieve a more accurate prediction of the thrust, the stall effect was incorporated into the model. For that, a critical angle of attack must be selected, above which stall is assumed to occur. This critical angle is noted as α_s.

We now need to develop the quadratic equation for the non-dimensional inflow, λ, once again. This time equating eq. 2.19 (which does not presume a linear lift relationship) with eq. 2.26, which results in

$$\sigma C_l r^3 dr = 4F\lambda(\lambda - \lambda_\infty)\, r\, dr \tag{2.32}$$

and after rearrangement

$$\lambda^2 - \lambda_\infty \lambda - \frac{\sigma C_l r^2}{4F} = 0 \tag{2.33}$$

whose solution is

$$\lambda = \frac{\lambda_\infty}{2} + \sqrt{\frac{\lambda_\infty^2}{4} + \frac{\sigma C_l r^2}{4F}} \tag{2.34}$$

where

$$C_l = \begin{cases} \dfrac{-\alpha_s C_{l,\alpha}}{\frac{\pi}{2} - \alpha_s}\alpha - \dfrac{\pi}{2} C_{l,\alpha} \dfrac{\alpha_s}{\frac{\pi}{2} - \alpha_s} & \text{if } \alpha \geq \dfrac{-\pi}{2} \text{ and } \alpha < -\alpha_s \\ C_{l,\alpha}\alpha & \text{if } \alpha \geq -\alpha_s \text{ and } \alpha \leq \alpha_s \\ \dfrac{-\alpha_s C_{l,\alpha}}{\frac{\pi}{2} - \alpha_s}\alpha + \dfrac{\pi}{2} C_{l,\alpha} \dfrac{\alpha_s}{\frac{\pi}{2} - \alpha_s} & \text{if } \alpha > \alpha_s \text{ and } \alpha \leq \dfrac{\pi}{2} \end{cases} \tag{2.35}$$

and $\alpha = \theta + \alpha_0 - \phi$.

Since C_l is a function of λ, because $\alpha = \alpha(\theta, \alpha_0, \phi)$ and $\phi = \phi(\lambda)$, this needs to be solved iteratively with eq. 2.34.

2.2 BEMT Including Swirl and without Small Angles Assumption

For some propellers the assumptions of no swirl and small angles can lead to an over prediction of the thrust and power, depending on its geometrical properties. The X8 propeller blade has a unique shape with high twist and large pitch angle. Because of that we will now develop a more sophisticated BEMT model that includes swirl and considers large angles, based on the model developed by Stahlhut[25].

The key difference between the model presented here and Stahlhut's model is that it is derived based on the *local* solidity, $\sigma = \frac{N_b c}{2\pi y}$, rather than *global* solidity as used by Stahlhut. In addition, the numerical approach used to solve the equations differed from Stahlhut's solution: whereas he used the bracketed-bisection method, the present work made use of the Matlab function *fsolve*, as will be briefly discussed later in section 2.2.2.

2.2.1 Blade element theory

Without the assumptions of no swirl and small angles we have the following velocities in the system,

$$V_P = V_\infty + v_i = V \sin\phi \tag{2.36}$$

$$V_T = \Omega y - u_i = V \cos\phi \tag{2.37}$$

Using eq. 2.1, 2.2, 2.5 and 2.16 we can write the thrust coefficient element as

$$\begin{aligned}
dC_T &= \frac{N_b \left(dL \cos\phi - dD \sin\phi\right)}{\rho\pi R^4 \Omega^2} \\
&= \frac{N_b \left(\frac{1}{2}\rho V^2 c\right) \left(C_l \cos\phi - C_d \sin\phi\right) dy}{\rho\pi R^4 \Omega^2} \\
&= \left(\frac{N_b c}{2\pi y}\right) y V^2 \left(\frac{C_l V_T - C_d V_P}{V R^4 \Omega^2}\right) dy \\
&= \sigma \frac{y}{R} \sqrt{V_T^2 + V_P^2} \left(\frac{C_l V_T - C_d V_P}{R^2 \Omega^2}\right) d\frac{y}{R} \\
&= \sigma \sqrt{\xi^2 + \lambda^2} \left(C_l \xi - C_d \lambda\right) r\, dr
\end{aligned} \tag{2.38}$$

where $\lambda = V_P/(\Omega R)$ is the non-dimensional inflow ratio and $\xi = V_T/(\Omega R)$ is the swirl (azimuthal) flow ratio. Similarly, the power coefficient element can be written as

$$\begin{aligned}
dC_P &= \frac{N_b\,(dL\sin\phi + dD\cos\phi)\,\Omega y}{\rho\pi R^5\Omega^3} \\
&= \frac{N_b\left(\frac{1}{2}\rho V^2 c\right)(C_l\sin\phi + C_d\cos\phi)\,\Omega y\,dy}{\rho\pi R^5\Omega^3} \\
&= \left(\frac{N_b c}{2\pi y}\right) y V^2 \left(\frac{C_l V_P + C_d V_T}{V R^5\Omega^2}\right) y\,dy \\
&= \sigma\sqrt{V_T^2 + V_P^2}\left(\frac{C_l V_P + C_d V_T}{R^2\Omega^2}\right)\frac{y^2}{R^2}\,d\frac{y}{R} \\
&= \sigma\sqrt{\xi^2 + \lambda^2}\,(C_l\lambda + C_d\xi)\,r^2\,dr.
\end{aligned} \tag{2.39}$$

2.2.2 Momentum theory

Once again, from the momentum theory we have

$$dC_T = 4|\lambda|\lambda_i r dr, \tag{2.40}$$

$$dC_P = 4|\lambda|\xi_i r^2 dr \tag{2.41}$$

where $\lambda_i = v_i/(\Omega R)$ and $\xi_i = u_i/(\Omega R)$.

Incorporating the tip losses without the small angle assumption leads to

$$dC_T = 4K_T|\lambda|\lambda_i r dr, \tag{2.42}$$

$$dC_P = 4K_P|\lambda|\xi_i r^2 dr \tag{2.43}$$

where $K_T = [1-(1-F)\cos\phi]$ and $K_P = [1-(1-F)\sin\phi]$ and

$$F = \frac{2}{\pi}\cos^{-1}\left[\exp\left(\frac{N_b\,(r-1)}{2r\sin\phi}\right)\right]. \tag{2.44}$$

Combining the results of power and thrust coefficients from momentum theory and BET, results in the following system of equations

$$\sigma\sqrt{\xi^2+\lambda^2}\,(C_l\xi - C_d\lambda)\,rdr = 4K_T|\lambda|\lambda_i rdr \tag{2.45}$$

$$\sigma\sqrt{\xi^2+\lambda^2}\,(C_l\lambda + C_d\xi)\,r^2dr = 4K_P|\lambda|\xi_i r^2dr. \tag{2.46}$$

In order to solve this system numerically, we first need to transform this system to the form of $G(x) = 0$:

$$\sigma\sqrt{\xi^2+\lambda^2}\,(C_l\xi - C_d\lambda) - 4K_T|\lambda|\lambda_i = 0 \tag{2.47}$$

$$\sigma\sqrt{\xi^2+\lambda^2}\,(C_l\lambda + C_d\xi) - 4K_P|\lambda|\xi_i = 0 \tag{2.48}$$

where $\lambda_i = \lambda - \lambda_\infty$ and $\xi_i = r - \xi$ such that,

$$\sigma\sqrt{\xi^2+\lambda^2}\,(C_l\xi - C_d\lambda) - 4K_T|\lambda|\,(\lambda-\lambda_\infty) = 0 \tag{2.49}$$

$$\sigma\sqrt{\xi^2+\lambda^2}\,(C_l\lambda + C_d\xi) - 4K_P|\lambda|\,(r-\xi) = 0 \tag{2.50}$$

and we can represent C_l as

$$C_l = C_{l,\alpha}\,(\theta+\alpha_0-\phi) \tag{2.51}$$

which leads to the following coupled system of equations

$$\sigma\sqrt{\xi^2+\lambda^2}\,\left[C_{l,\alpha}\,(\theta+\alpha_0-\phi)\,\xi - C_d\lambda\right] - 4K_T|\lambda|\,(\lambda-\lambda_\infty) = 0 \tag{2.52}$$

$$\sigma\sqrt{\xi^2+\lambda^2}\,\left[C_{l,\alpha}\,(\theta+\alpha_0-\phi)\,\lambda + C_d\xi\right] - 4K_P|\lambda|\,(r-\xi) = 0 \tag{2.53}$$

where

$$\phi = \tan^{-1}\left(\frac{\lambda}{\xi}\right). \tag{2.54}$$

This system of equations can be solved numerically for λ and ξ.

One way to verify this system of two equations is by applying the assumptions of small angles and no swirl after the fact, and comparing it to the model that assumed small angles and no swirl a priori. With the assumptions of small angles and no swirl we have

$$\lambda^2 \approx 0 \tag{2.55}$$

$$\xi \approx r \tag{2.56}$$

$$C_d\lambda \approx 0, \tag{2.57}$$

since we also assume that the drag is very small. Using these in eqs. 2.52 and 2.53 leads to the same form as with the assumption of no swirl and with small angles a priori (eq. 2.20 and 2.21), which validates the development of this model.

2.3 BEMT Including Swirl and with Small Angles Assumption

To further investigate the affect of the assumption of small angles and swirl, we now assume only small angles but do include the swirl. With the assumption of small angles we have

$$\lambda^2 \approx 0 \tag{2.58}$$

$$C_d\lambda \approx 0, \tag{2.59}$$

since we also assume that the drag is very small.

With that we obtain

$$\sigma\xi^2 C_{l,\alpha}(\theta+\alpha_0-\phi)-4K_T|\lambda|(\lambda-\lambda_\infty)=0 \tag{2.60}$$

$$\sigma\xi\left(C_{l,\alpha}(\theta+\alpha_0-\phi)\lambda+C_d\xi\right)-4K_P|\lambda|(r-\xi)=0. \tag{2.61}$$

2.4 Single Rotor Experiments

In order to validate the results of the simulation, it was considered essential to also measure the thrust and torque produced by various propellers, and compare those to our simulated results. In order to measure the thrust and torque of a propeller for a given rotational speed, a custom-made test-stand was built.

2.4.1 RPM-Thrust-Torque test-stand

The test stand, shown in Fig. 2–2, enables the measurement of a single small propeller and includes (a) an ATI Gamma 6-axis Force/torque sensor; (b) an aluminum shaft to attach the motor, resulting in distance of 0.38 meter from the sensor's reference frame to the motor's shaft; (c) a Rimfire 400 Outrunner Brushless DC Motor; (d) a FlyFun-18A electronic speed controller (ESC); (e) an ArduPilot Mega micro-controller[1]; (f) an Optical RPM sensor for eLogger V4[2]; and (g) an Eagle Tree eLogger V4. The motor is oriented in such way that the thrust can be measured using the T_y axis of the sensor by $T=\frac{T_y}{l}$ where l represents the test-stand arm, which is the distance between the sensor's reference frame and the motor's shaft. Note that the thrust can also be measured using the F_x axis but with

[1] `https://code.google.com/p/ardupilot-mega/wiki/Hardware`

[2] `http://dev.eagletreesystems.com/index.php?route=product/product&product_id=71`

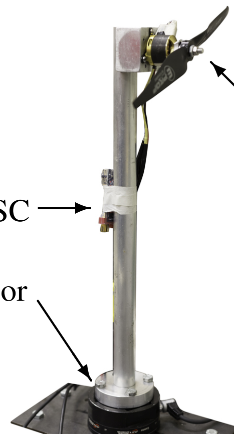

Figure 2–2: Test-stand for single rotors

less accuracy since the values measured by F_x utilize smaller percentage of the sensor's full-scale load. The motor torque can be measured using the T_x axis by simply $Q = T_x$.

According to the sensor's calibration certificate and accuracy report (performed by ATI Industrial Automation), the T_y axis has a maximum error of 1.25% of 100lbf-in (the full-scale load), which, in combination with the test-stand arm, is translated to an error of approximately ± 0.37N. Similarly, the T_x axis has a maximum error of 1% of 100lbf-in, which is translated to an error of approximately ± 0.11Nm.

2.4.2 Test-stand operation

Using the test-stand, the thrust and torque values were measured at various rotational speeds. For each rotational speed, a command was sent to the controller which, via the ESC, rotated the propeller for approximately 10 seconds while the RPM, thrust and torque values were recorded only when the system reached its steady state. Since the Eagle Tree eLogger V4 RPM sensor has a sample rate of 50Hz, the number of measured RPM values can reach to a few hundred, depending the specified rotational speed. In addition, the ATI

F/T sensor has a sample rate of 7.8KHz, which can result in tens of thousands thrust and torque values. An averaging filter is used on all measured values in order to minimize the effect of any noise that may occur. Only a single data point is then retained from each test.

2.4.3 Thrust and torque measurements credibility

In order to validate the credibility of our test-stand results, thrust and torque were measured for 2 propellers (APC14x12, APC10x4.7SF) and compared with the wind tunnel measurements from the University of Illinois at Urbana-Champaign (UIUC) Airfoil Database[3]. These two propellers were selected from the UIUC database because they are both designed for small UAVs that operate at a similar range of Reynolds numbers as the X8 (up to approximately $\mathrm{Re} = 100,000$).

Since the UIUC data is presented in the non-dimensional form as thrust and power coefficients (C_t and C_p, respectively), it must be dimensionalized using the relations

$$T = C_t \rho n^2 D^4$$
$$P = C_p \rho n^3 D^5$$
$$Q = \frac{P}{2\pi n}$$

where $n = \frac{\Omega}{2\pi}\left[\frac{\mathrm{rev}}{\mathrm{s}}\right]$ and $D = 2R$.

In Fig. 2–3a, one can see that the thrust measurements done with our test-stand are similar to those obtained from UIUC measurements. Similarly, Fig. 2–3b, shows that our torque measurements are comparable to those of UIUC, even though some scatter in the

[3] `http://aerospace.illinois.edu/m-selig/ads.html`

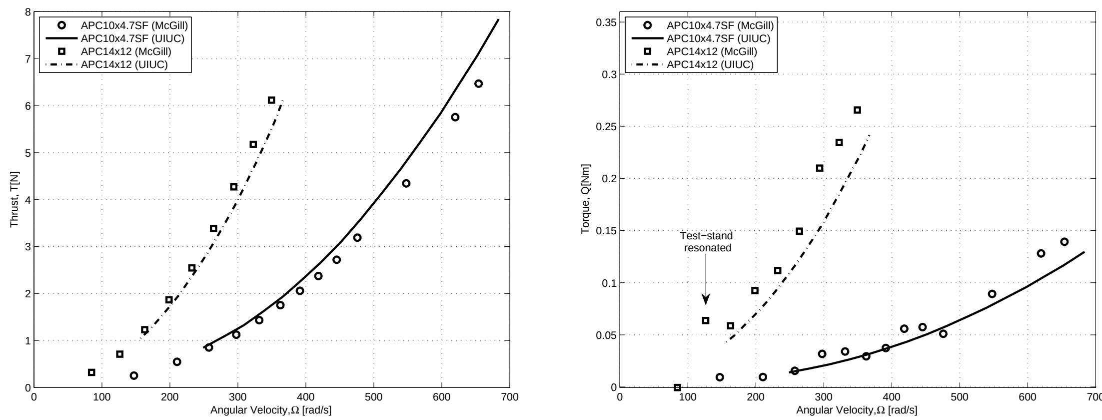

(a) Thrust (b) Torque

Figure 2–3: Test stand credibility, compared to UIUC Airfoil Database

test-stand torque measurements is present. This scatter is likely being caused by the vibrations occurring in the test-stand during operation, combined with the low torque values measured that utilize only a small percentage of the full-scale load of the force/torque sensor, as discussed in section 2.4.1. In addition, the torque values being measured range only from 1 to 2 times the error specifications of the sensor. It is also possible for a systematic difference to exist between our torque results and those of UIUC, if the motors used had significantly different internal friction characteristics.

These results validate the thrust and torque measurements credibility of our test-stand, thus allowing the use of the test-stand measurements for comparisons and validations in this thesis.

2.5 Blade Aerodynamic Characteristics

In order to implement the developed BEMT model for thrust and torque prediction of a specific rotor, the geometric and aerodynamic characteristics of the propeller must be obtained at several radial locations of the blade along its radius. These characteristics include the chord length c, pitch angle θ, 2-D lift curve slope $C_{l,\alpha}$, zero-lift angle α_0 and the drag coefficient C_d.

2.5.1 Radius and chord

The chord length at each radial location can be measured using a caliper, measuring from the leading-edge to the trailing-edge. These radial locations can be measured using a measuring tape or, as done in this study, by reading the grid of a millimeter graph paper glued onto the blade as seen in Fig 2–4.

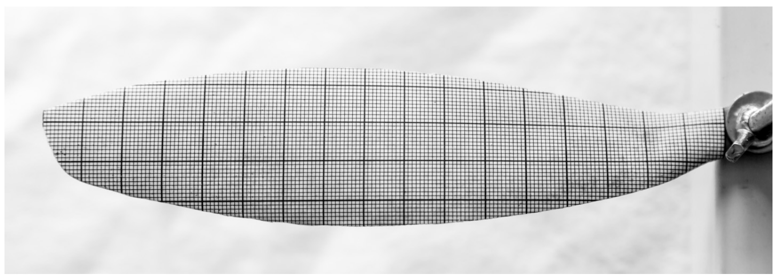

Figure 2–4: Radial location using millimeter graph paper

2.5.2 Pitch angle

The pitch angle can be measured by slicing the propeller into pieces (elements). The propeller is first mounted onto a straight rectangular bar, which will be used as a reference line. Then it is cut at several radial locations. The cut is done perpendicular to the radius and the cross-cut is painted to increase its contrast relative to its surrounding. A digital photo is taken for each cut, capturing the airfoil shape (see Fig. 2–5). These photos are analyzed in a graphical software (e.g. GIMP[26]) to manually trace the airfoil shape (as a Bézier curve). The pitch angle can be calculated from the airfoil orientation (i.e. chord orientation), relative to the reference line and can be also done using the graphical

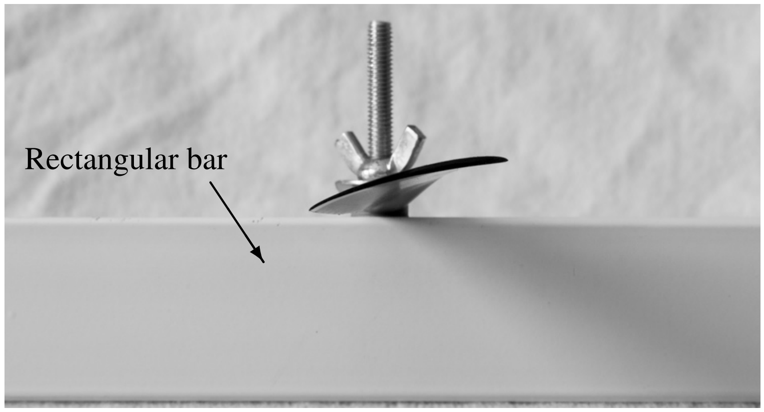

Figure 2–5: Propeller mounted and cut

software. An example of a series of airfoils from the APC16x5.5MR propeller, and their orientations, can be viewed in Fig. 2–6.

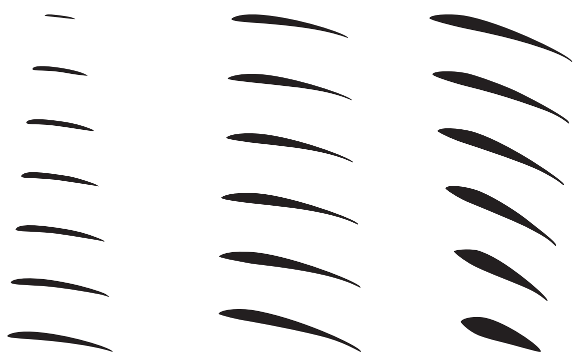

Figure 2–6: APC16x5.5MR airfoils

Each airfoil is exported as a black and white raster image which is then imported into a software called Profili™, which can convert the airfoil image to a coordinate file. Using these coordinates, the thickness and mean camber line can also be extracted.

2.5.3 2-D lift curve slope

The 2-D lift curve slope is not measured but simply assumed, without serious loss of accuracy[1], to be constant for an incompressible flow. In the present work we assume a value of 2π, which is obtained from thin-airfoil theory.

2.5.4 Zero-lift angle

For cambered (i.e. non-symmetrical) airfoils, the zero-lift angle α_0 has a large impact on the predicted thrust in the BEMT model. Moreover, it is difficult to obtain a precise zero-lift angle value. Hence, it is important to find the most accurate method of estimating its value. The zero-lift angle can be obtained by the following three methods:

- Calculation using the assumption of a thin circular arc airfoil[27] by $\alpha_0 = 2\frac{z}{c}$, where z is the maximum camber.
- Simulation using MIT's XFOIL software[28][29][26], based on the airfoil coordinates. XFOIL is an interactive program for the design and analysis of subsonic isolated airfoils that uses a potential flow solution, coupled with an integral boundary layer. XFOIL is commonly used and has been proven to be an accurate utility for airfoil design and analysis[30][31].
- Calculation using thin airfoil theory[32] which is based on the shape of the camber line.

In order to select the best method, the zero-lift angle was obtained for a dozen cambered airfoils for which experimental wind tunnel lift measurements were available (see Fig. 2–7), using the three different methods.

In tables 2–1 and 2–2 the obtained zero-lift angles are compared to wind tunnel measurements[33][34] of the airfoils at a Reynolds number of 100K, and at higher Reynolds numbers. Values closest to the experimentally-measured angle are shown in bold font. The airfoils are sorted ascending by maximum camber ratio.

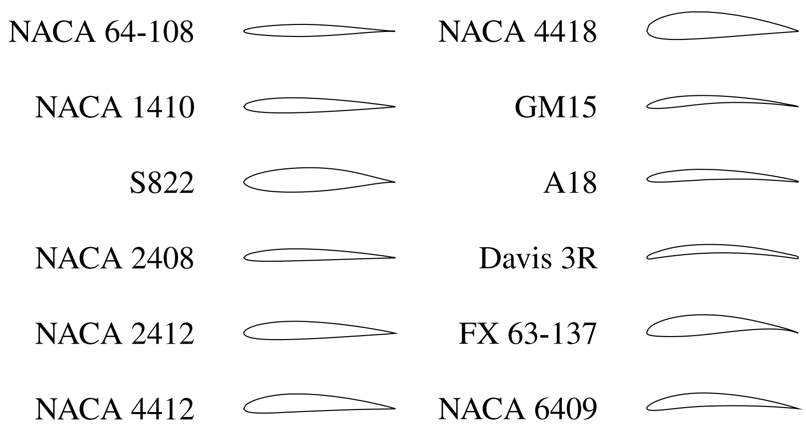

Figure 2–7: Airfoils

Table 2–1: Zero-lift angle methods comparison for Reynolds = 100,000

Airfoil	Meas.[deg]	Thin Circular Arc	XFOIL	Thin Airfoil Theory
S822	-0.83	2.18	**-1.35**	2.72
GM15	4.00	5.45	**2.62**	5.56
A18	2.70	5.78	**2.61**	4.41
Davis 3R	3.10	6.77	**2.65**	6.23
FX 63-137	5.00	6.82	**4.56**	9.10
NACA 6409	4.00	6.88	**3.73**	6.16

While the simplest method for calculating the zero-lift angle is the thin circular arc assumption, this method was found to be the least accurate, especially at low Reynolds numbers. However, at high Reynolds and high maximum camber ratio it showed an advantage over the thin airfoil theory.

As expected, the classical thin theory method, which is more complex than the thin circular arc method, is usually the most accurate for slightly cambered airfoils at high

Table 2–2: Zero-lift angle methods comparison for high Reynolds number

Airfoil	Re[10^3]	Meas.[deg]	Thin Circular Arc	XFOIL	Thin Airfoil Theory
NACA 64-108	500	0.40	**0.63**	0.90	0.88
NACA 1410	500	1.00	1.15	1.14	**1.02**
S822	500	2.34	2.18	**2.41**	2.72
NACA 2408	500	2.00	2.29	2.24	**2.05**
NACA 2412	500	2.10	2.29	2.30	**2.03**
NACA 4412	500	3.90	4.58	4.22	**3.88**
NACA 4418	500	3.90	4.58	4.41	**4.00**
A18	300	3.80	5.78	**3.47**	4.41
FX 63-137	500	7.00	**6.82**	8.50	9.10

Reynolds numbers. However, it fails to calculate the correct zero-lift angle when camber increases and Reynolds number decreases.

While XFOIL is particularly applicable to low Reynolds number airfoils[28], both thin circular arc and classic airfoil theory methods seem to be more accurate than the XFOIL simulation at high Reynolds numbers. However, the last two methods are not suitable for obtaining the zero-lift angle at low Reynolds numbers. This is mainly due to the fact that these two methods do not take the Reynolds number into account in their calculations.

Still, for low and high Reynolds numbers, the XFOIL method can have an error as large as $\approx 1.5°$, compared to the measured value. This error can result in approximately $\pm 15\%$ error in thrust prediction.

The above methods were also applied on all elements of 3 different propellers of small UAVs. These are the APC14x4.7SF, APC16x5.5MR and Draganflyer X4-P.

When comparing the 3 methods, it was found again that for the small UAV propellers (which typically operate at low Reynolds numbers) there can be a large discrepancies between the obtained zero-lift angles. An example of this variation can be seen in Fig. 2–8 for the APC16x5.5MR propeller. It is also clear that the obtained zero-lift angles are

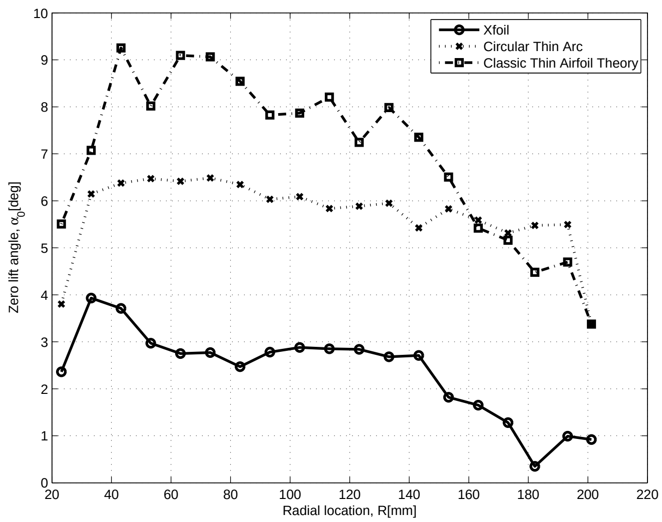

Figure 2–8: APC16x5.5MR Zero-lift angle per airfoil

not continuous along the radius of the propeller. The continuity problem is due to the sensitivity of the measurements of the captured airfoils shapes of each element. This can be overcome by fitting a smooth curve to represent the zero-lift angle distribution.

Although the zero-lift angles, obtained using XFOIL simulation, may have an error (as shown above), it was found to be the best method for small UAV propellers which operate at low Reynolds number.

It is important to note that the XFOIL simulation method is sensitive to the airfoil shape, expressed as the coordinate file. These coordinates determine the curvature of the airfoils (second derivative of the airfoil coordinates) which must be continuous. The smoother the curvature, the better the XFOIL simulation. In addition, in the airfoil's coordinate file, the trailing edge must be either sharp or open, otherwise XFOIL will not converge to a solution. This means that for some airfoils, with non-sharp trailing edge, the coordinate file must be modified to have an open trailing edge (referred as ”blunt trailing-edge” in XFOIL).

2.5.5 Drag coefficient

The drag coefficient can also be obtained by simulation using the XFOIL software, based on the airfoil coordinates. For simplicity, the drag coefficient profile is obtained only for the airfoil section located at approximately 3/4 of the propeller blade radius, and is assumed to be the same for other sections along the radius.

A curve is then fit through these simulated drag coefficient values to find an equation to represent the drag coefficient using the quadratic equation suggested by Bailey[35], in the form,

$$C_d = C_{d0} + d_1\alpha' + d_2\alpha'^2 \tag{2.62}$$

where, since the drag coefficient was obtained with XFOIL's simulation[4], $\alpha' = \alpha - \alpha_0$ or simply $\alpha' = \theta - \phi$.

2.6 Single Rotor Simulation Validation for the Hover Case

Once the aerodynamic characteristics of a rotor are known, the developed BEMT models can be used to simulate the thrust of the rotor for different rotational speeds by using 100 radial locations[3] along the rotor's blade. These simulations can then be compared to the experimental measurements from our test-stand.

---

[4] α' is in degrees and not rad/s.

2.6.1 Lift coefficient reduction due to stall

First, let us show whether incorporation of stall in the BEMT model indeed causes a reduction in the simulated lift coefficient. Figures 2–9a to 2–9d show distribution of lift coefficient over the non-dimensional radius for four different rotors, with critical angle assumed to be $\alpha_s = 12°$. We can see that the stall occurs only for two rotors, the

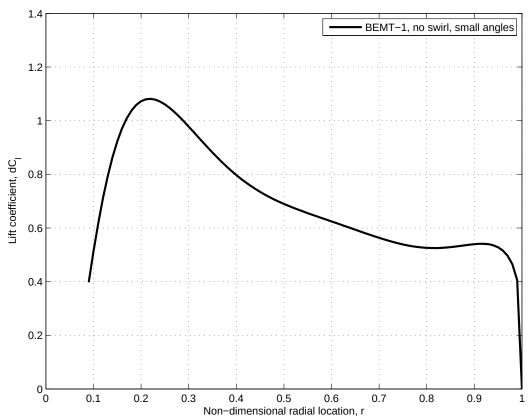

(a) APC14x4.7SF

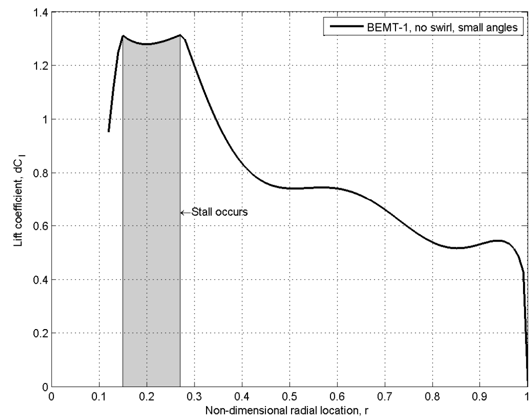

(b) APC16x5.5MR

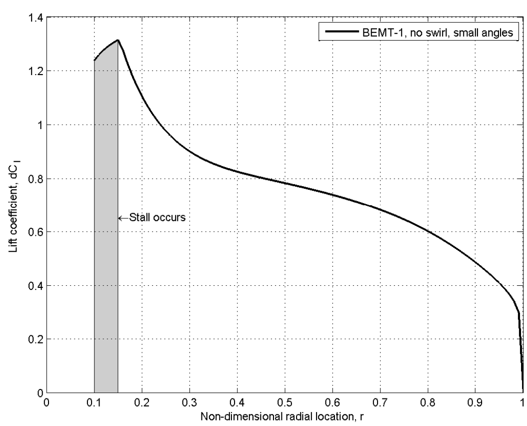

(c) X8

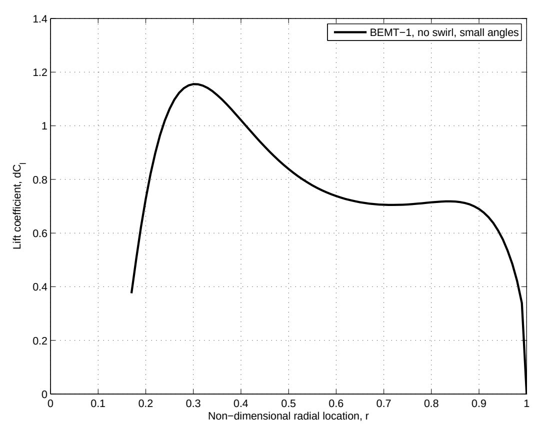

(d) X4-P

Figure 2–9: Lift coefficient distribution due to stall - Single rotor

APC16x5.5MR and the X8. In these rotors, the stall effects only a small section along the radius of the rotors' blades. Moreover, these sections are located very close to the root of the rotors, which is an area of the blade that is known to not affect the performance in a significant way.

With the above information we can now see how the thrust was affected by the reduction in lift coefficient due to stall. For that we chose to simulate only the thrust for the APC16x5.5MR, which, according to Figure 2–9b, seems to have the largest reduction in lift coefficient due to stall. Figure 2–10 shows comparison between simulated thrust with and without stall in the model. As expected, the stall causes an insignificant thrust

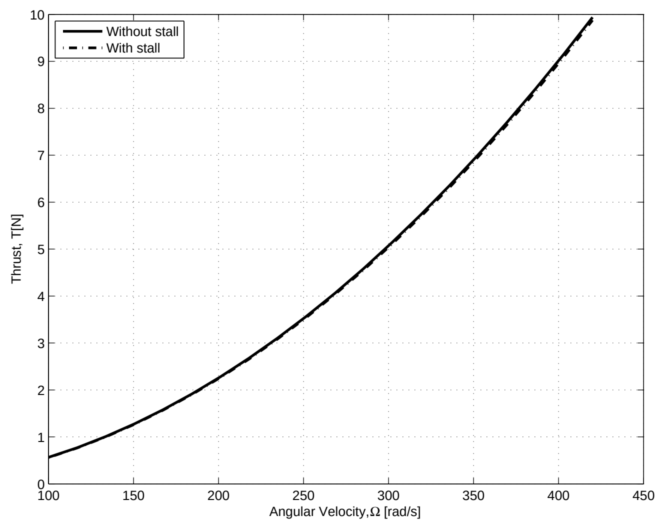

Figure 2–10: APC16x5.5MR simulated thrust, with and without stall

reduction, due to the minor reduction in lift coefficient.

For this reason, the stall was assumed to be negligible for all future simulations in this work.

2.6.2 Thrust simulations vs. measurements

Figures 2–11a to 2–11d show thrust simulation validation for four rotors.

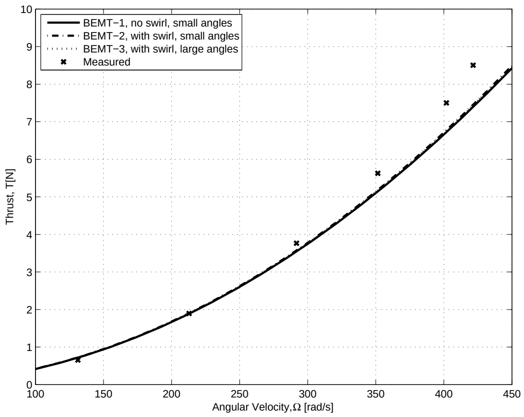

(a) APC14x4.7SF

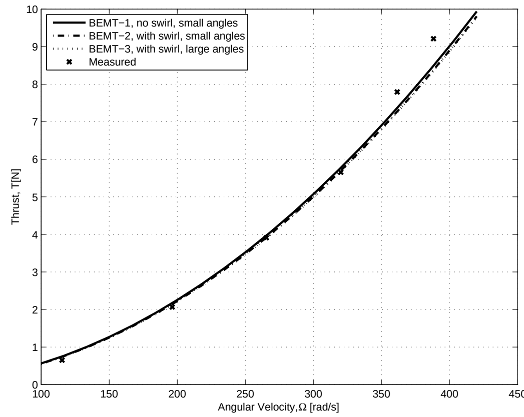

(b) APC16x5.5MR

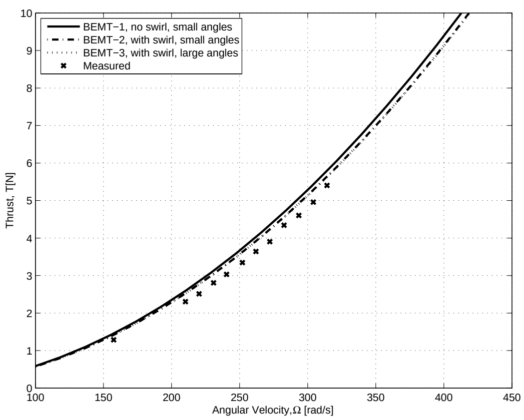

(c) X8

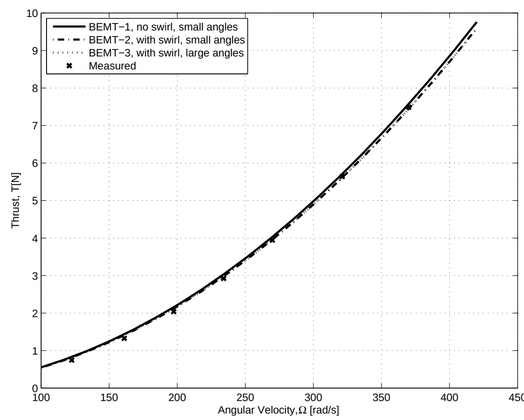

(d) X4-P

Figure 2–11: Thrust validation - Single rotor

Looking first at the simulations alone in the four plots we can see that the BEMT-2 (including swirl and *with* small angles assumption) model and BEMT-3 (including swirl and *without* small angles assumption) model are nearly the same. This suggests that the assumption of small angles has no visible effect on the results for these rotors in the hover case.

In addition, we can see that the simulation of the BEMT-1 (ignoring swirl and with small angle assumption) model is very similar to the simulations of the more comprehensive BEMT-2 and BEMT-3 models, for all four rotors. This is not surprising since the plots in Figure 2–11 are for the hover case, while BEMT-3 was proven to show better prediction mainly at higher advance-ratio values[25]. The similarities between the different simulations imply that there is no apparent advantage using the more comprehensive models that incorporate swirl. The largest difference between the BEMT-1 simulation to BEMT-2 and BEMT-3 simulations was observed for the X8 rotor. This is reasonable, given the X8's unique shape (see Fig. 2–12), which results in higher drag values. However, this difference still does not justify the added complication of the BEMT model.

(a) Front

(b) Top

Figure 2–12: X8 rotor

Importantly, for all four rotors, it can be noticed that the maximum error between the simulations and the measured thrusts is less than 15%. This error might be due to the inaccuracy of the obtained zero-lift angle, as discussed in section 2.5.4; but could also be result of the ±0.37N error specification on the measured thrust.

2.7 Axial Flight Simulation

The BEMT can also be used to simulate how the propeller will behave in axial flight. The easiest way to present the effect of axial flight, is to show a non-dimensional relationship between the thrust coefficient C_T and the climb inflow rate, λ_∞.

In order to validate axial flight simulation, we need some experimental data for comparison. Wind-tunnel measurements of axial flight were performed at UIUC for the APC10x4.7SF propeller. However, before comparing axial flight simulation and measurements, let us first validate our thrust prediction for the hover case for this propeller, which is shown in Fig. 2–13. In this plot we compare our simulation of the BEMT-1 model with

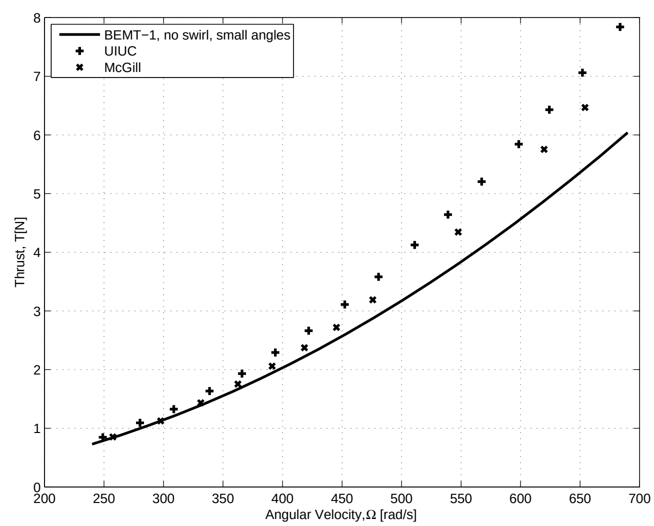

Figure 2–13: APC10x4.7SF thrust prediction vs. measurements for the hover case

two sets of experimental data, one was measured using our test-stand and the other was obtained from wind-tunnel measurements performed at UIUC. We can see that the simulation under-predicts both sets of measurements. This under-prediction may be due to error in the estimated zero-lift angle (e.g., a 3-4 degree increase in the zero-lift angle, as predicted by the method that assumes thin circular arc airfoil, results in a much better match). Considering this discrepancy, we will nevertheless continue to simulate and validate the axial flight.

The axial flight wind-tunnel measurements performed at UIUC are presented by a relationship between thrust coefficient, $C_t = T/\left(\rho n^2 D^4\right)$, and advance ratio, $J = V_\infty/(nD)$. However, the definitions for these non-dimensional values are different from our definitions. For that we need to convert our simulation to the same form where advance ratio is $J = \lambda_\infty \pi$, and the thrust coefficient is $C_t = C_T \pi^3/4$.

A simulation for the APC10x4.7SF axial flight, using the BEMT-1 model, is shown in Fig. 2–14. As expected, for advance ratio of $J = 0$ (i.e. hover case), the simulation

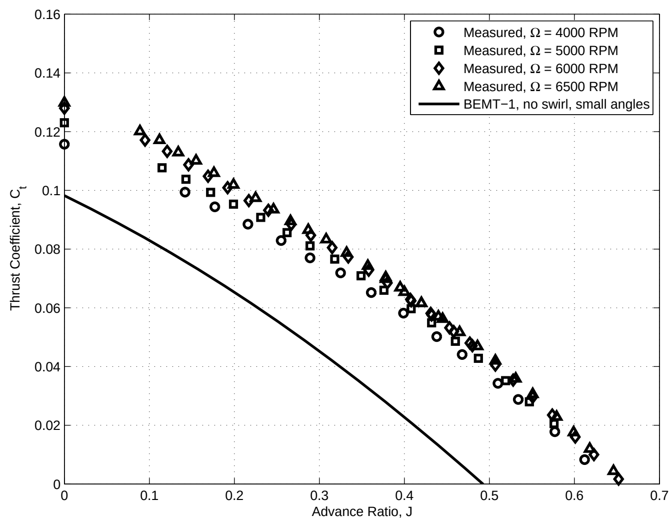

Figure 2–14: APC10x4.7SF thrust coefficient vs. advance ratio

under-predicts the UIUC wind-tunnel measurements of the thrust coefficient. However, the simulation follows the same trend as the experiments, with increasing advance ratio.

This indicates that, for a simulation that correctly predicts the thrust in the hover case, there would likely be a good match at higher advance ratios.

Chapter 3
Coaxial-Rotor Modeling and Experiments

In helicopters, coaxial-rotor configuration can be described as a thruster having two counter-rotating rotors operating on the same axis, producing the thrust to fly the vehicle. An illustration for a helicopter with coaxial-rotor is shown in Fig. 3–1. Due to this config-

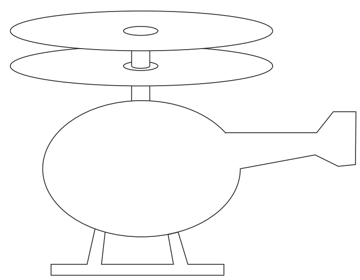

Figure 3–1: Helicopter with a coaxial-rotor

uration, a tail-rotor is not required to counteract the torque reaction of the main rotor (i.e. maintain torque-balanced condition) during flight. In addition, a helicopter with coaxial-rotor can usually carry more payload compared to conventional helicopters of the same size.

3.1 BEMT for the Coaxial-Rotor

As stated in Chapter 1, coaxial-rotor systems require more power in order to produce the same total thrust as two single independent rotors. This indicates that a flow interaction between the upper and lower rotors, in the coaxial-rotor system, affects its performance. Understanding and considering this interaction, is the key to developing a proper model to simulate coaxial-rotor systems.

In this chapter we will take the developed BEMT-1 model for the single rotor from Chapter 2 and, along with few assumptions, modify it to include the contribution of the additional (i.e. lower) rotor in the system. The development of this BEMT coaxial-rotor model is mainly based on the model developed by Leishman and Ananthan[3] which was designed for full size coaxial-rotors, that are operated with the upper and lower rotors spinning at equal and opposite speeds. In this configuration a collective pitch (as discussed in Chapter 1) for non-twisted upper and lower rotor blades is used to maintain a torque-balanced condition. In addition, their model uses global solidity, which can be easily calculated for non-twisted, linearly tapered blades. Therefore, we will do some minor enhancements to Leishman and Ananthan's model in order to adapt it to our case, since small UAV rotors (twisted or not), typically have fixed pitch blades, and the rotational speed of the two rotors is not equal and can vary significantly during operation. In addition, we will use a local solidity in our model, similar to what is done in Chapter 2.

3.1.1 BEMT assumptions for the coaxial-rotor

In addition to the assumptions made for the development of our BEMT model for a single rotor, a few more assumptions are required for a coaxial-rotors configuration. We can use Fig. 3–2 in order to better understand the assumptions about the flow through the coaxial-rotor. First we assume that the upper and lower rotors are spaced sufficiently far apart to prevent inter-rotor blade collisions. Second, we assume that the upper rotor affects the flow into the lower rotor while the lower rotor does not affect the upper rotor. Third, we make the assumption that the lower rotor operates partially in the fully developed slipstream (i.e. vena-contracta) of the upper rotor in which the wake from the upper rotor contracts to $r_c \approx 0.8$. While this is slightly higher than the value $r_c = \sqrt{0.5}$ predicted by

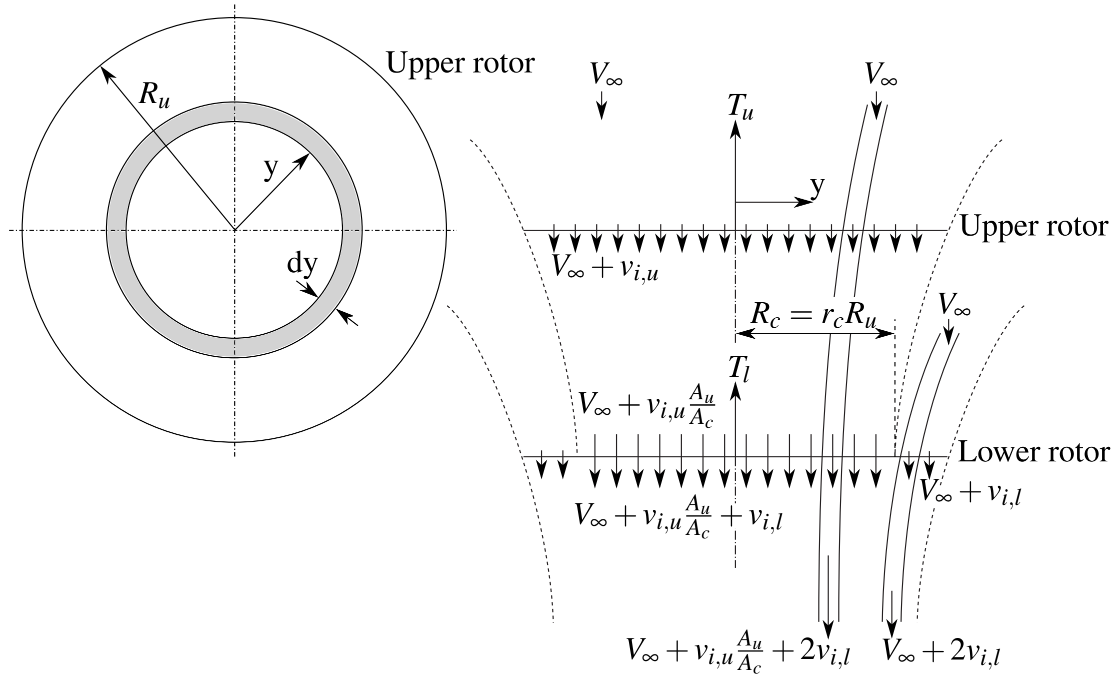

Figure 3–2: Flow diagram for coaxial-rotor

momentum theory, it has been found to be more representative of the true value that occurs relatively quickly downstream (within $0.25R$) of the upper rotor[3]. This assumption, along with continuity equation, is translated into a climbing (i.e. axial) velocity of the lower rotor of $V_{\infty,l} = V_\infty + v_{i,u}(A_u/A_c)$ where A_u is the area of the upper rotor disk and $A_c = \pi(r_c R_u)^2$ is the area of the contracted wake of the upper rotor at the lower rotor plane.

Since part of the lower rotor area is affected by the flow from the upper rotor, different set of equations is developed for the part of the rotor operating in that contracted area. The area of the lower rotor which is outside the upper rotor's vena-contracta is solved using the same equations as for the upper rotor (i.e. as a single rotor).

3.1.2 BEMT for the upper rotor

Following the assumption that the upper rotor is not affected by the lower rotor, we can use the same method developed for the single rotor in section 2.1 to calculate the inflow according to,

$$\lambda_u = \sqrt{\left(\frac{\sigma_u C_{l,\alpha,u}}{8F} r - \frac{\lambda_{\infty,u}}{2}\right)^2 + \frac{\sigma_u C_{l,\alpha,u}}{4F} \left(\theta_u + \alpha_{0,u}\right) r^2} - \left(\frac{\sigma_u C_{l,\alpha,u}}{8F} r - \frac{\lambda_{\infty,u}}{2}\right) \tag{3.1}$$

from which the thrust and power coefficients of the upper rotor can be calculated using eq. 2.20 and 2.21. Note the subscript X_u, which represents the upper rotor.

3.1.3 BEMT developed for lower rotor

Momentum theory

We now need to develop equations for the thrust produced by a propeller annulus, while accounting for the modified incoming flow for $r \leq r_c$.

From momentum theory, with the previously-stated assumptions, the mass flow rate through an annulus for $r \leq r_c$ is

$$d\dot{m} = \rho \left(V_\infty + v_{i,u}\frac{A_u}{A_c} + v_{i,l}\right) 2\pi y_l \, dy_l \tag{3.2}$$

where $v_{i,u}\frac{A_u}{A_c}$ is the induced velocity in the contracted area at the lower rotor, produced by the upper rotor, and $v_{i,l}$ is the induced velocity produced by the lower rotor.

The incremental thrust over the annulus is then $2v_{i,l}d\dot{m}$ which can be expressed as

$$dT_l = 2\rho \left(V_\infty + v_{i,u}\frac{A_u}{A_c} + v_{i,l}\right) v_{i,l} 2\pi y_l \, dy_l. \tag{3.3}$$

From the thrust coefficient definition in eq. 2.16 and eq. 3.3 we get

$$
\begin{aligned}
dC_{T,l} &= \frac{dT_l}{\rho\pi R_l^4 \Omega_l^2} \\
&= \frac{4\pi\rho\left(V_\infty + v_{i,u}\frac{A_u}{A_c} + v_{i,l}\right) v_{i,l} y_l \, dy_l}{\rho\pi R_l^4 \Omega_l^2} \\
&= \frac{4\left(V_\infty + v_{i,u}\frac{A_u}{A_c} + v_{i,l}\right) v_{i,l} y_l \, dy_l}{R_l^4 \Omega_l^2}
\end{aligned} \tag{3.4}
$$

and in non-dimensional form

$$
\begin{aligned}
dC_{T,l} &= 4\left(\lambda_{\infty,l} + \lambda_{i,u}\frac{A_u}{A_c}\frac{\Omega_u}{\Omega_l}\frac{R_u}{R_l} + \lambda_{i,l}\right)\lambda_{i,l} r \, dr \\
&= 4\left(\lambda_{\infty,l} + (\lambda_u - \lambda_{\infty,u})\frac{1}{r_c^2}\Omega_r R_r + \lambda_{i,l}\right)\lambda_{i,l} r \, dr
\end{aligned} \tag{3.5}
$$

where induced inflow ratio of upper rotor is $\lambda_{i,u} = \lambda_u - \lambda_{\infty,u}$, climbing speed ratio of lower rotor is $\lambda_{\infty,l} = \frac{V_\infty}{\Omega_l R_l}$, contracted area ratio is $\frac{A_u}{A_c} = \frac{1}{r_c^2}$, rotational speed ratio is $\Omega_r = \frac{\Omega_u}{\Omega_l}$, radii ratio is $R_r = \frac{R_u}{R_l}$ and induced inflow ratio of lower rotor is $\lambda_{i,l} = \frac{v_{i,l}}{\Omega_l R_l}$.

Now, lets denote

$$\lambda_{\infty,c} = \lambda_{\infty,l} + (\lambda_u - \lambda_{\infty,u})\frac{1}{r_c^2}\Omega_r R_r, \tag{3.6}$$

$$\lambda_{l,c} = \lambda_{\infty,c} + \lambda_{i,l} \tag{3.7}$$

and after rearrangement we have

$$\lambda_{i,l} = \lambda_{l,c} - \lambda_{\infty,c} \tag{3.8}$$

which yields

$$dC_{T_l} = 4\left(\lambda_{\infty,c} + \lambda_{l,c} - \lambda_{\infty,c}\right)\left(\lambda_{l,c} - \lambda_{\infty,c}\right) r dr \tag{3.9}$$

$$= 4\lambda_{l,c}\left(\lambda_{l,c} - \lambda_{\infty,c}\right) r dr. \tag{3.10}$$

Applying the tip-loss factor leads to

$$dC_{T,l} = 4F\lambda_{l,c}\left(\lambda_{l,c} - \lambda_{\infty,c}\right) r dr. \tag{3.11}$$

Blade element theory

Again, in similar way to the single rotor development, using eq. 2.20, the incremental thrust produced over the annulus is

$$dC_{T,l} = \sigma_l C_{l,\alpha}\left(\left(\theta_l + \alpha_{0,l}\right) r - \lambda_{l,c}\right) r^2 dr. \tag{3.12}$$

Equating the two equations from the BET, eq. 3.12 , and the momentum theory, eq. 3.11, we get

$$\sigma_l C_{l,\alpha}\left(\left(\theta_l + \alpha_{0_l}\right) r - \lambda_{l,c}\right) r = 4F\lambda_{l,c}\left(\lambda_{l,c} - \lambda_{\infty,c}\right) \tag{3.13}$$

and then rearranging

$$\lambda_{l,c}^2 + \lambda_{l,c}\left(\frac{\sigma_l C_{l,\alpha}}{4F} r - \lambda_{\infty,c}\right) - \frac{\sigma_l C_{l,\alpha}}{F}\left(\theta_l + \alpha_{0,l}\right) r^2 = 0. \tag{3.14}$$

The solution for this quadratic equation is

$$\lambda_{l,c} = \sqrt{\left(\frac{\sigma_l C_{l,\alpha}}{8F} r - \frac{\lambda_{\infty,c}}{2}\right)^2 + \frac{\sigma_l C_{l,\alpha}}{4F}\left(\theta_l + \alpha_{0,l}\right) r^2} - \left(\frac{\sigma_l C_{l,\alpha}}{8F} r - \frac{\lambda_{\infty,c}}{2}\right). \tag{3.15}$$

The outer part of the lower rotor is not affected by the prop-wash of the upper rotor. To account for this, for $r > r_c$, the solution is similar to the upper rotor, given by eq. 3.1,

$$\lambda_l = \sqrt{\left(\frac{\sigma_l C_{l,\alpha}}{8F} r - \frac{\lambda_{\infty,l}}{2}\right)^2 + \frac{\sigma_l C_{l,\alpha}}{4F}\left(\theta_l + \alpha_{0,l}\right) r^2} - \left(\frac{\sigma_l C_{l,\alpha}}{8F} r - \frac{\lambda_{\infty,l}}{2}\right). \tag{3.16}$$

where $\lambda_{\infty,l} = \frac{V_\infty}{\Omega_l R_l}$.

As stated before, we assume that the upper rotor is not affected by the lower rotor. However, the lower rotor *is* affected by the upper rotor (where $r \leq r_c$), i.e. $\lambda_{l,c} = \lambda_{l,c}(\lambda_u)$. Thus, the inflow of the upper rotor, λ_u must be solved first by using eq. 3.1 and then the inflow of the lower rotor under the contracted area, $\lambda_{l,c}$, can be solved using eq. 3.15. In addition, the inflow of the lower rotor, λ_l, where $r > r_c$ can be solved independently, using eq. 3.16, since it is not affected by the upper rotor.

Once λ_u and λ_l and $\lambda_{l,c}$ are known, the elemental thrust coefficients of the upper rotor and of the lower rotor can be calculated using eq. 2.20, namely

$$dC_T = \sigma C_{l,\alpha}\left(\left(\theta + \alpha_0\right) r - \lambda\right) r^2 dr,$$

where λ is substituted by λ_u, λ_l or $\lambda_{l,c}$, as necessary.

The elemental thrust coefficients are then integrated to calculate $C_{T,u}$ and $C_{T,l}$ of the upper and lower rotors. These thrust coefficients are then dimensionalized to calculate the total thrust of the coaxial pair, using

$$T_{coax} = C_{T,u}\rho\pi R_u^4 \Omega_u^2 + C_{T,l}\rho\pi R_l^4 \Omega_l^2. \tag{3.17}$$

Similarly, the coaxial-rotor net torque is the difference between the upper and lower rotor torque values, evaluated as follows

$$Q_{coax} = C_{Q,u}\rho\pi R_u^5\Omega_u^2 - C_{Q,l}\rho\pi R_l^5\Omega_l^2. \tag{3.18}$$

However, in order to calculate the *total* torque required by the coaxial-rotor system (for purpose of calculating power consumption), the summation of the absolute torque values should be performed.

3.1.4 BEMT model validation using Harrington rotor 1

In order to validate the developed BEMT model for coaxial-rotors, a performance simulation of the previously tested Harrington rotor 1[14], was done. For this purpose, its aerodynamic characteristics are required. Knowing the rotor has no twist nor camber and using its geometrical properties, captured from Harrington's paper (shown in Figure 3–3), we can deduce its chord and pitch angle distributions and zero lift angle (which is zero due to the absence of camber). In addition, the viscous drag coefficients are selected to be similar to those in Leishman's[3] paper, gathered from Syal[22]. These coefficients are $C_{d0} = 0.11$, $d_1 = 0.021$ and $d_2 = 0.65$, based on NACA 0012 airfoil section measurements so that the drag coefficient is

$$C_d = 0.11 + 0.021\alpha + 0.65\alpha^2. \tag{3.19}$$

This drag coefficient profile was used in the current work for consistency with Leishman and Ananthan's[3][18] results. Note that the angle α is used in eq. 3.19, rather than α' as in eq. 2.62 because $\alpha_0 = 0$ for this symmetric airfoil section. Note also that the coefficients in the quadratic equation are for α in radians rather than degrees.

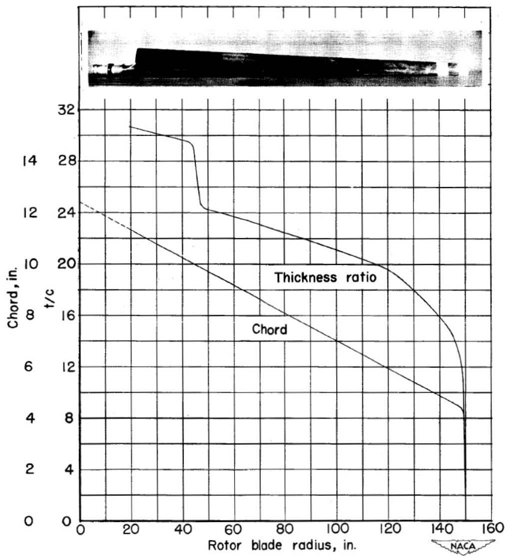

Figure 3–3: Harrington Rotor 1: Chord c and thickness ratio t/c along the radius r

With the above aerodynamic characteristics, the thrust and power coefficient are calculated by

$$C_{T,coax} = C_{T,u} + C_{T,l}$$

$$C_{P,coax} = C_{P,u} + C_{P,l}$$

which is permitted only since for the Harrington rotor 1 the torque-balance condition is maintained for *equal* rotational speeds, $\Omega_u = \Omega_l$ (while using different pitch angles for the upper and lower rotors, such that $\theta_u = 8.1597°$ and $\theta_l = 8.6547°$, based on Syal[22]). The simulation of the thrust and power coefficients is compared to Harrington's experimental measurements for validity, shown in Fig. 3–4.

We can see that the simulation done with the BEMT for coaxial-rotor agrees very well with Harrington's measurements, although for high power values, the simulation tends

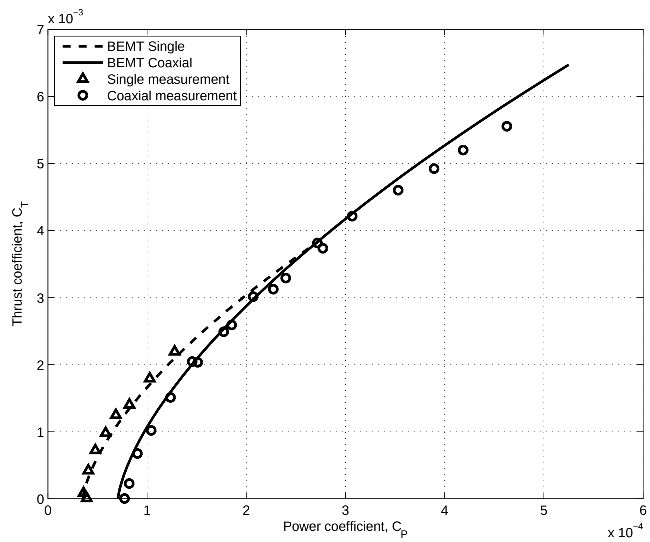

Figure 3–4: Harrington Rotor 1: Simulation compared to measurements

to over-predict the thrust. This result is consistent with Leishman's simulation and is considered satisfactory.

3.2 Coaxial-Rotor Experiments

3.2.1 Test-stand components for the coaxial propellers

As mentioned earlier, a small UAV typically maintains a torque-balanced condition by rotating the upper and lower rotors at different speeds. Moreover, during maneuvers, the rotational speed ratio between the upper and the lower rotors varies significantly. In order to measure the performance of coaxial-rotor that operates in these rotational speeds ratios, a new test-stand (rather than the single rotor test-stand) was built to allow controlling and measuring the rotational speeds of the two motors simultaneously and also measuring the total produced thrust and net torque of the coaxial-rotor. The coaxial test-stand, see Fig. 3–5, enables the measurement of a coaxial propeller pair and, in contrast to the single rotor test-stand, includes two Turnigy Aerodrive SK3 4240-530kv brushless motors (operated by one 4-cell Lithium-Polymer 5400 mAh 14.8 V battery), two Electronic Speed Controllers (ESC)[1], two RPM optical detectors / phototransistors (QRD1114) and a PIC18F13K22 micro-controller.

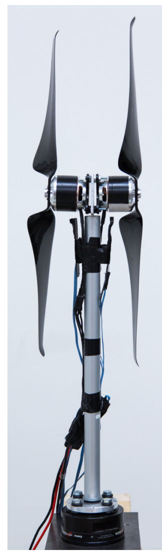

Figure 3–5: Coaxial-rotor test-stand

On the X8 UAV, there is an angle of approximately 4.5° between the two rotors (in the coaxial-rotor), shown in Fig. 3–6. Our test-stand was built similarly in order to replicate this construction from the X8 frame.

3.2.2 Coaxial-rotor test-stand operation

During the coaxial-rotor experiment, the motors were rotated at a set of several upper and lower rotors speed combinations. An array of thrust measurements with each element

[1] http://www.mikrokopter.de/ucwiki/en/BL-Ctrl_2.0

Figure 3–6: X8 pod

value corresponding to different rotational speed combination of upper and lower rotors was measured. In Fig. 3–7 we can see 3-D plots of variation in thrust and torque values for the various rotational speeds of the upper and lower rotors of the APC16x5.5MR and X8 Coaxial-rotors.

We can see from the plots in Figs. 3–7a and 3–7b of the thrust measurements for the two coaxial-rotors that, as expected, the highest thrust can be achieved when both rotors are spinning at their highest speed. A closer examination of the data reveals that the APC16x5.5MR produces approximately 0.5N more thrust than the X8 for the same rotational speeds. Interestingly, for the cases where $\Omega_r \neq 1$, higher thrust is achieved when $a = \Omega_l > \Omega_u = b$ than when $b = \Omega_l < \Omega_u = a$. That is, the lower rotor rotates faster than the upper rotor, rather than the reverse case, for the same speed values a and b.

In order to further analyze the effect of the different rotational speeds combinations of upper and lower rotors on the measured thrust and net torque we plot these measurements vs. the rotational speed ratio, Ω_r, as can be viewed in Fig. 3–8.

In these plots we can see that the behaviour observed in Fig. 3–7 is stronger with the X8 coaxial-rotor, i.e. higher thrust is achieved for $\Omega_r < 1$, for the same speed values a and b as mentioned before. In addition we see from Fig. 3–8d that for the X8 coaxial-rotor,

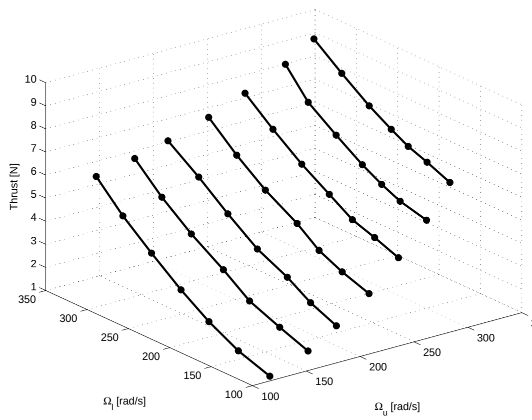

(a) APC16x5.5MR - Thrust

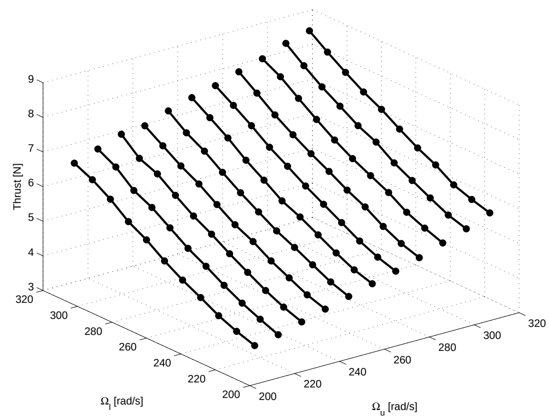

(b) X8 - Thrust

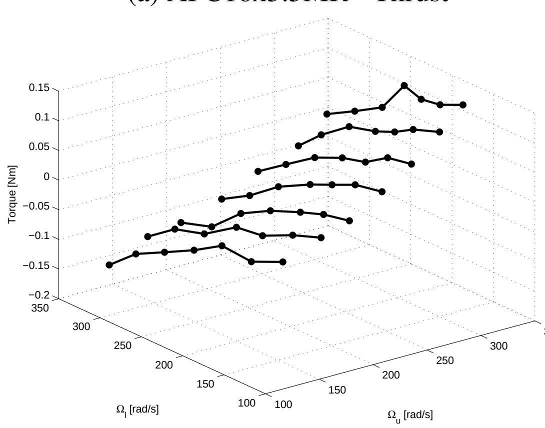

(c) APC16x5.5MR - Torque

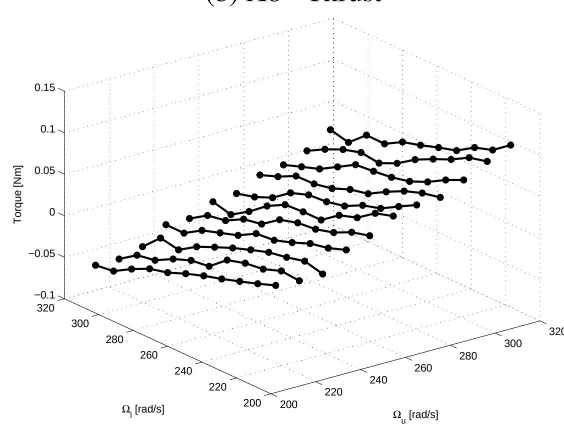

(d) X8 - Torque

Figure 3–7: Thrust and torque measurements vs. upper and lower rotors' rotational speed - Coaxial-rotors

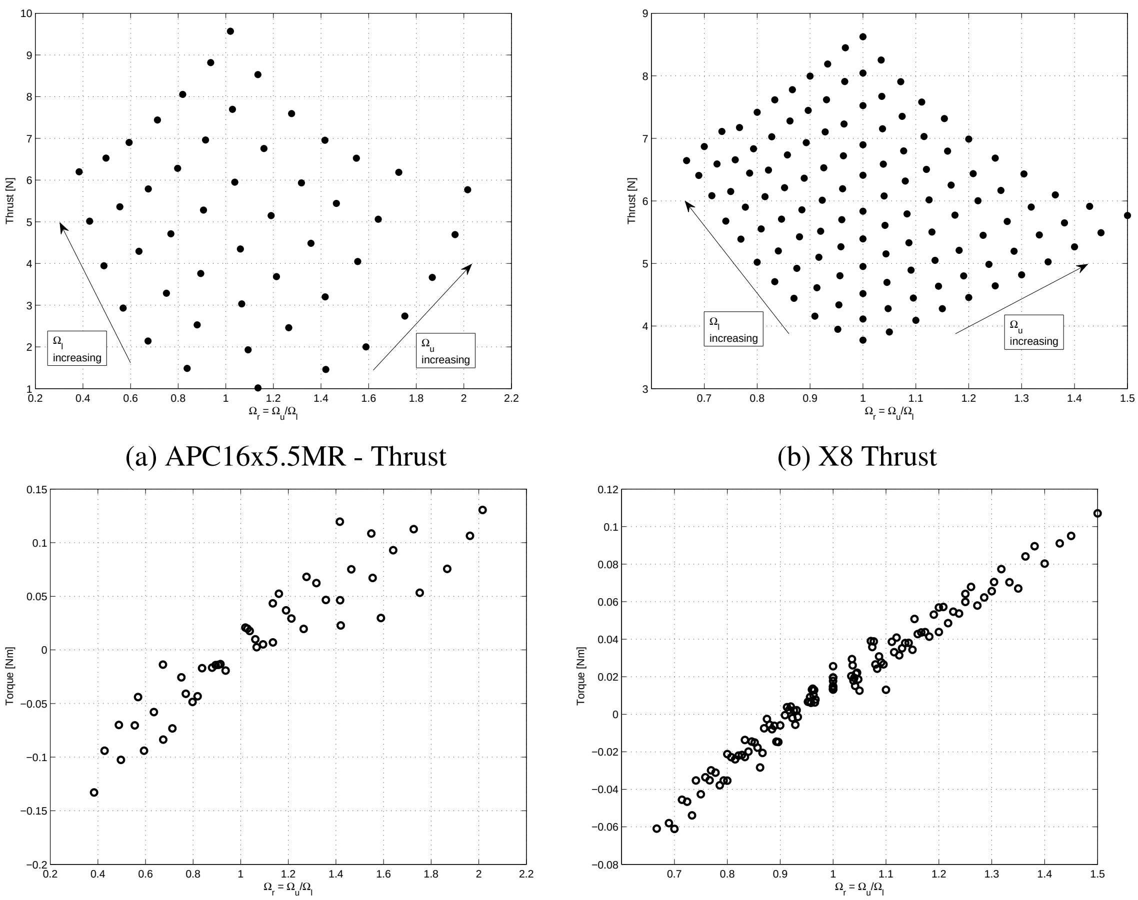

(a) APC16x5.5MR - Thrust

(b) X8 Thrust

(c) APC16x5.5MR - Torque

(d) X8 - Torque

Figure 3–8: Thrust and torque measurements vs. rotational speed ratio - Coaxial-rotors the torque-balanced condition is met when $\Omega_r \approx 0.9$, whereas for the APC16x5.5MR it is met when $\Omega_r \approx 1$.

Due to non-uniform spacing between measured rotational speeds of upper and lower rotors, it is impossible to plot a surface figure, showing the measured thrust and torque over Ω_u and Ω_l, which can be compared to the BEMT model simulation. For this reason, the *scatteredInterpolant* function was used in Matlab to produce matrix of thrust values for uniform-spaced upper and lower rotational speeds of the same range as measured (i.e. without extrapolating). The measured-interpolated thrust data for APC16x5.5MR and X8 appears in Fig. 3–9. We can see that the uniform-spaced interpolated data, shown in Fig.

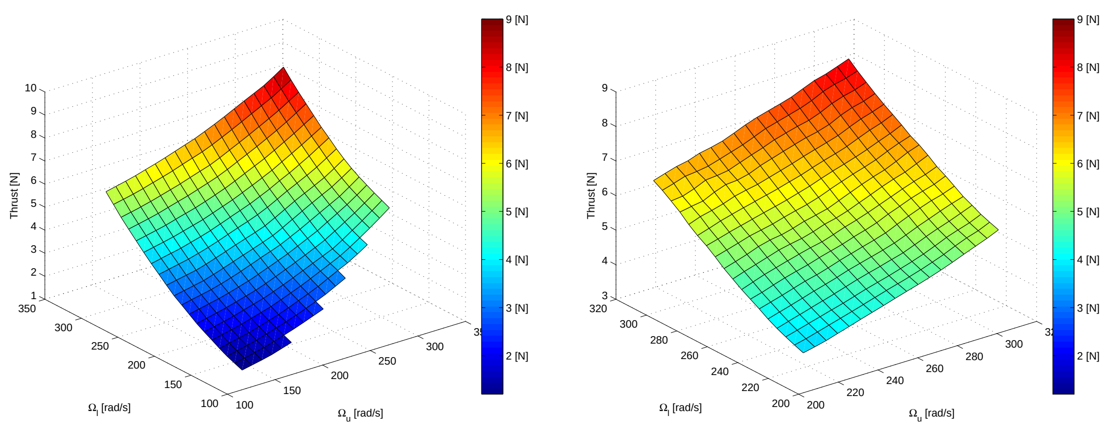

(a) APC16x5.5MR - Thrust

(b) X8 - Thrust

Figure 3–9: Thrust interpolated-measurements - Coaxial-rotors

3–9, is similar to the real measured data, shown in Fig. 3–7.

3.3 Coaxial-Rotor Simulation Validation for the Hover Case

The obvious way to visually validate and analyze the prediction of the BEMT model for coaxial-rotor is by plotting the simulated and measured thrusts on the same graph, as shown in Fig. 3–10. However, as stated earlier, reading accurately this kind of represen-

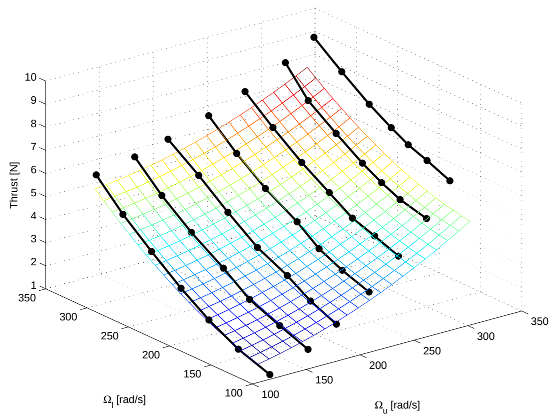

(a) APC16x5.5MR

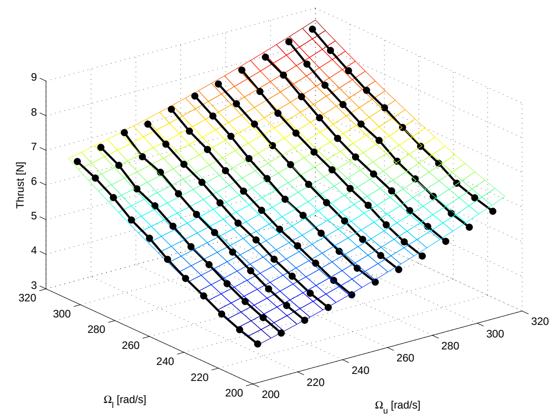

(b) X8

Figure 3–10: Simulation (mesh) and measured (lines) thrusts - Coaxial-rotor

tation is difficult. For that reason we instead calculate the error of the predicted thrust using,

$$T_{Err} = \frac{T_{predicted} - T_{measured}}{T_{measured}} \cdot 100 \tag{3.20}$$

where the measured thrust is actually the interpolated-measured thrust. With this calculation we present the thrust prediction error for the APC16x5.5MR and X8 rotors, as shown in Fig. 3–11.

The plots in Fig. 3–11 show variation in error of thrust prediction, compared to measured thrust, for various combinations in rotational speeds of the upper and lower rotors. The range of rotational speeds in the plots was set to be similar for both rotors for an

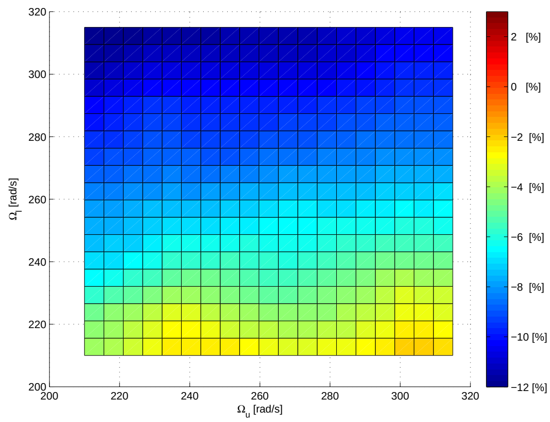

(a) APC16x5.5MR

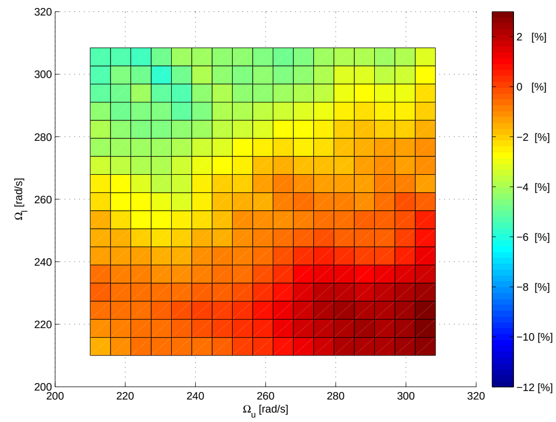

(b) X8

Figure 3–11: Thrust simulation error - Coaxial-rotor

easier comparison. It is important to note that in these tests (and simulations), the torque-balanced condition was not enforced, in order to mimic the conditions of operation. However, even without considering the torque-balanced condition, we can see that the simulation for the two coaxial-rotors predicts well the measured thrusts with error ranging from approximately -5% to +3% for the X8 and -12% to -2% for the APC16x5.5MR.

In the X8 coaxial-rotor we can generally see that the error is at its minimum when the upper rotor rotates faster than the lower rotor. In particular, the error is smallest when the upper rotor rotates approximately 20 rad/s faster than the lower rotor. This condition is somewhat similar to the in-flight hovering measurements done with the X8 by Sharf[36]. It was observed that during operation, the upper rotor always rotates faster than the lower rotor with up to approximately 10 rad/s difference. This means that our model should predict very well the thrust during flight operation.

We can see, for both coaxial-rotors, that the lower rotor has a much larger effect on the error compared to the upper rotor, and this is more obvious for the APC16x5.5MR rotor. Specifically, we can see that for high rotational speeds of the lower rotor, the simulation under-predicts the thrust, with an error of approximately 11%. This is true regardless of the rotational speed of the upper rotor, although there is slight improvement in thrust prediction when the upper rotor rotates faster. By contrast, we can see that for the APC16x5.5MR coaxial-rotor, for low rotational speeds of the lower rotor, the simulation under-predicts the thrust, by approximately 2% to 4%. In this case, the error decreases as the upper rotor rotates faster.

3.4 Propeller Alternatives

When viewing the X8 UAV, one cannot ignore the unique shape of its propellers. Draganfly, the manufacturer of the X8, states in its website[2] that "*The Draganflyer X8 UAV helicopter features a unique design that minimizes thrust lost to sound output. The rotor blades have been designed for maximum efficiency while naturally producing less turbulence when spinning*".

We were interested to investigate this issue more carefully. In the field of propeller design, which has been studied for more than several decades, a unique shape does not necessarily result in a more efficient design. In particular, we wanted to critically evaluate the claim that the X8 propeller's unique design minimizes the thrust loss for maximum efficiency. To do this, we searched for off-the-shelf propellers with similar diameter and pitch to compare to the X8. To narrow the search, we chose propellers only from the Advanced

[2] `http://www.draganfly.com/uav-helicopter/draganflyer-x8/features/`

Precision Composites (APC) line of products as they are readily available. Considering the diameter and pitch, three propellers were selected after reading through the APC Propeller Performance Data[3], which shows simulated results for different rotational speeds. The selected propellers are the APC14x4.7SF Slow-Flyer, APC14x5N Sports-Prop (where N stands for narrow) and APC16x5.5MR Multi-Rotor. Their simulated thrusts comparison can be seen in Fig. 3–12. From this simulated data we can see that the APC14x.47SF and

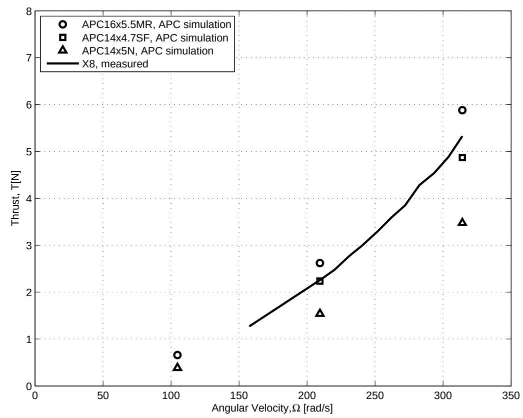

Figure 3–12: APC's simulated thrust vs. rotational speed data for comparison between selected propellers

APC16x5.5MR rotors are predicted to produce equal or greater thrust compared to the X8, while the APC14x5N is predicted to produce lower thrust. However, considering the fact that this is merely a simulated data, we chose all these propellers for comparison.

Draganfly has recently ceased to produce or support the X8. Their closest replacement vehicle is the X4-P which has a conventional quad-rotor configuration. Therefore,

[3] http://www.apcprop.com/v/downloads/PERFILES_WEB/datalist.asp

the propeller of the X4-P was added to the comparison. Interestingly, the X4-P propeller appears to have a more conventional design than the X8.

In this section, we present performance results for the X8 and the four propeller alternatives. These are shown first for a single rotor, followed by results for a coaxial-rotor pair.

3.4.1 Single rotor thrust and torque measurements comparison

From Fig. 3–13a, showing the thrust comparison of the selected propellers, it is obvious that the APC14x5N and APC14x4.7SF propellers (both are 14” in diameter) produce less thrust than the 16” X8 propeller unless they are spun at much higher speeds. By contrast, the two other 16” propellers, namely the APC16x5.5MR and the X4-P, produce thrust which is similar to the X8.

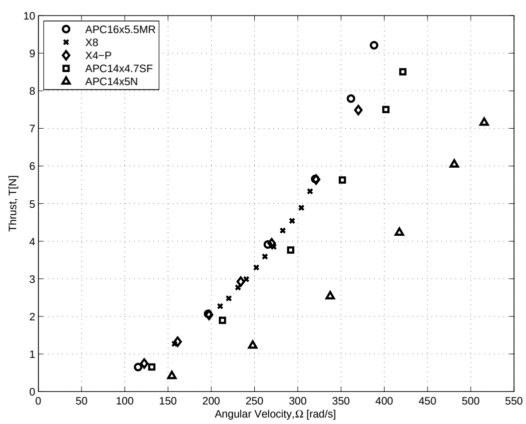

(a) Thrust vs. rotational speed

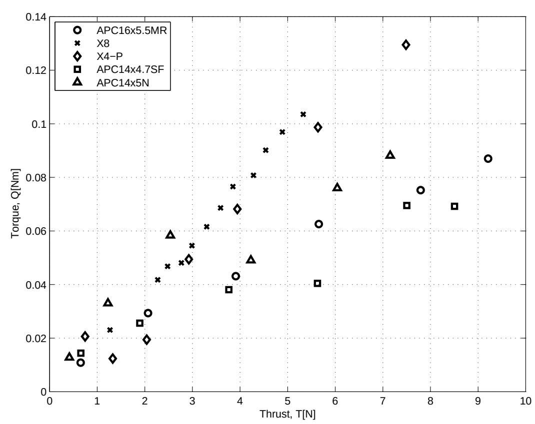

(b) Thrust vs. torque

Figure 3–13: Thrust vs. rotational speed and torque comparison for selected propellers - Single rotor

However, when considering the thrust vs. torque measurements, presented in Fig. 3–13b, it is clear that the APC14x4.7SF and APC16x5.5MR are more efficient than the two Draganfly propellers since they require less torque to produce similar thrust.

Considering these results, we can conclude that the APC16x5.5MR performs as well as the X8 prop, and is also the most efficient of all propellers considered for the single rotor configuration. The relatively poor performance of the X8 propeller, from the perspective of torque vs. thrust, calls into question the Draganfly efficiency claims.

Apart from the performance advantages of the APC16x5.5MR propeller, it is also cheaper and costs $7.5 since it is mass-produced an made of inexpensive plastic, while the X8 propeller is custom-made out of costly carbon fiber and costs $200. However, being made out of plastic, makes the APC16x5.5MR heavier than the X8 propeller (43g vs. 18g, respectively). Assuming a quad-rotor configuration (i.e. 4 rotors), translates to the APC16x5.5MR contributing approximately additional 10% of total weight of the vehicle, compared to approximately 4% that the X8 contributes.

Taking all these factors into account, the APC16x5.5MR is considered to be the better compromise for a small quad-rotor UAV.

3.4.2 Coaxial-rotor thrust and torque measurements comparison

It was suggested that the unique shape of the X8 propellers might have an advantage in the coaxial arrangement so another comparison was done for this configuration. For that, a *pusher* propeller of the same model of each propeller, driven by a second motor and located underneath it, was mounted downstream of the first rotor. In this coaxial-rotor configuration, the pusher is practically the lower rotor and with a mirror shape (i.e. reverse pitch) of the upper rotor that rotates in the opposite direction to the upper rotor. This evaluation could only be performed for the propellers that have a matching pusher propeller, i.e. the APC16x5.5MR and the APC14x4.7SF. The APC14x5N and X4-P propellers are not made with a reverse pitch. The results are shown in Fig. 3–14. In these tests, the rotational speeds of the upper and lower rotors were set to be equal to simplify the presentation of the comparison.

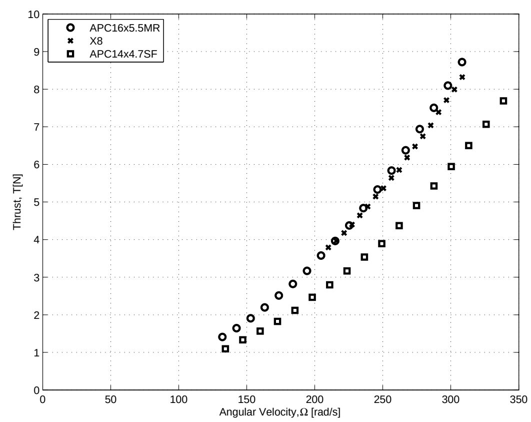

Figure 3–14: Thrust vs. rotational speed for the coaxial configuration

Similarly to the single-rotor results, the thrust produced by the APC14x4.7SF in the coaxial-rotor configuration is smaller than the X8 and requires to be spun approximately 50 rad/s faster to achieve the same thrust. Moreover, since the APC14x4.7SF requires less torque for the same thrust as the X8, as shown in Fig. 3–13b, it can indeed be spun faster and still require less torque, without stressing the motors.

Because the two propellers in the coaxial-rotor configuration are mounted on the same force/torque sensor, it was not possible to measure the torque required from each motor. Only the net torque could be measured due to the fact that the two propellers are counter-rotating. However, considering the results from the single-rotor comparison, one can assume that similar torque vs. thrust trend will occur in the coaxial-rotor case. This is supported by Leishman[3] who has analytically showed that the coaxial-rotor requires approximately 22% more power to produce the same thrust of two separated single rotors combined. In addition, we can use the BEMT model to evaluate the total torque (i.e. the sum of the absolute values of the upper and lower rotor torques) vs. thrust of the coaxial-rotors, shown in Fig. 3–15. This simulation, similarly to the single-rotor experiments,

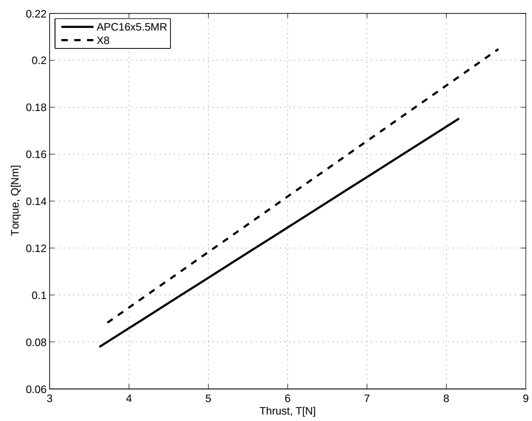

Figure 3–15: Predicted torque vs, thrust for the coaxial-rotor

predicts that the APC16x5.5MR will require less torque in order to produce the same thrust as the X8 rotor.

With this information, combined with the thrust measurements presented in Fig. 3–14, it can concluded that the APC16x5.5MR in the coaxial-rotor configuration is the most efficient propeller.

Again, when considering the performance advantages and cost, it is apparent that the APC16x5.5MR may be a better choice for the coaxial-rotor pair configuration for the X8 UAV.

During the DRDC project to convert the Draganflyer X8 to an autonomous UAV we realized that the payload weight capability of the vehicle is higher than required for the task. Because of that, and following the information we recently received from Draganfly Inc. that the X8 will not be supported in the future, we have decided to convert the X8 frame to its new replacement in the Draganfly Inc. line of products, the Draganflyer X4-P. As mentioned before, the X4-P is a UAV with quad-rotor configuration. However, following the findings showed in section 3.4.1 it is clear that the APC16x5.5MR is the better choice for its performance, even in a quad-rotor configuration. Yet, using rotors that are not produced by Draganfly means the warranty of the UAV may be voided. In addition, the new X4-P propellers are significantly cheaper than the X8 propeller and cost only $50 per rotor. This means that since the quad-rotor requires only 4 rotors then the cost issue has a lesser impact on the decision to use other alternatives. Hence for the time being, we will be using the X4-P rotors on the X8 frame (converted to quad-rotor) and not the better performing APC16x5.5MR.

Chapter 4
Operation in Ground Effect

It is well known that hovering and flying with proximity to large objects alters the flow into the rotor or the development of the rotor wake. One of the main subjects of this type investigated is the *ground effect*, which was initially studied by Küssner[37] and Betz[38]. It was noticed that proximity to the ground with distance smaller than one radius of the rotor, given a constant power, had a large impact on the produced thrust. Alternatively, the ground effect can also be viewed as an effect that reduces the power required to produce the same thrust as in out of ground effect. This fact enabled early human powered helicopters to hover above the ground, even though they did not have enough power to rise out of the ground effect.

As a result of the increased thrust for a constant power, the ground effect is regularly exploited by pilots during landing, which acts as a cushion for descending helicopters when approaching the ground. For this reason, it is very important to understand the behaviour of a thruster in presence of the ground effect, when developing a controller for autonomous landing of a UAV.

At this point in our investigation, a decision had been taken that future work on this project would continue with the X4-P configuration, shown in Fig. 4–1. As such, this investigation into ground effect was undertaken with that propeller only.

Figure 4–1: Draganflyer X4-P

Moreover, since the BEMT model does not explicitly consider the flow downstream of the propeller, it cannot be used to predict ground effect. As such, this investigation was purely experimental.

4.1 Ground Effect Modeling for the Single Rotor

Many researchers have studied the ground effect and have developed models to predict the produced thrust in ground effect. One of the most commonly used was developed by Cheeseman and Bennett[39], which represents the rotor as a source and uses the method of images to consider the ground as a streamline. This approach yields the result that the induced velocity at the rotor is reduced by an amount $\Delta v_i = v_i \left(\frac{R}{4Z}\right)^2$ due to the presence of the ground plane, where v_i represents the induced velocity at the rotor, out of ground effect. Cheeseman and Bennett then consider the case where the same power is consumed in and out of ground effect, i.e. $T_{OGE} v_i = T_{IGE} \left(v_i - \Delta v_i\right)$, thereby leading to

$$\left[\frac{T_{IGE}}{T_{OGE}}\right]_{P=\text{Const}} = \frac{1}{1-\left(\frac{R}{4Z}\right)^2} = \frac{1}{k_G}, \tag{4.1}$$

where T_{IGE} and T_{OGE} are the thrusts in ground effect and out of ground effect, respectively, and Z is the distance from the ground. Cheeseman's result is based on the assumptions that the power is the same in and out of ground effect and that the induced velocity is constant along the rotor's radius. Simulation of ground effect, using Cheeseman's formula, for constant power is shown in Fig. 4–2.

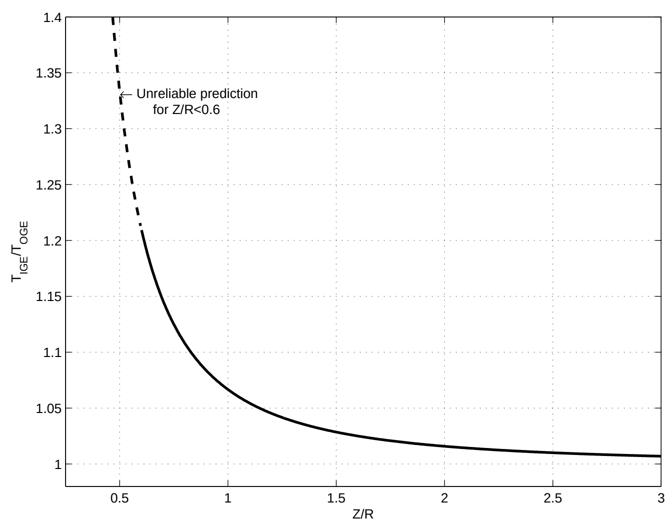

Figure 4–2: Variation of thrust in ground effect for constant power by Cheeseman

Rather than assuming that the power consumed is the same in and out of ground effect, it is possible to instead consider the case where the thrust is the same at these two conditions. In this case, we have $P_{OGE} = T v_i$ and $P_{IGE} = T\,(v_i - \Delta v_i)$. We can then take the ratio of these two powers to find

$$\left[\frac{P_{IGE}}{P_{OGE}}\right]_{T=\text{Const}} = \frac{v_i - \Delta v_i}{v_i} = 1 - \left(\frac{R}{4Z}\right)^2 = k_G. \tag{4.2}$$

Comparing eq. 4.1 to eq. 4.2 we can see that

$$\left[\frac{P_{IGE}}{P_{OGE}}\right]_{T=\text{Const}} = \left[\frac{T_{OGE}}{T_{IGE}}\right]_{P=\text{Const}} = 1 - \left(\frac{R}{4Z}\right)^2, \tag{4.3}$$

which predicts the reduction in required power for constant thrust. Simulation of ground effect, using Cheeseman's formula, for constant thrust is shown in Fig. 4–3.

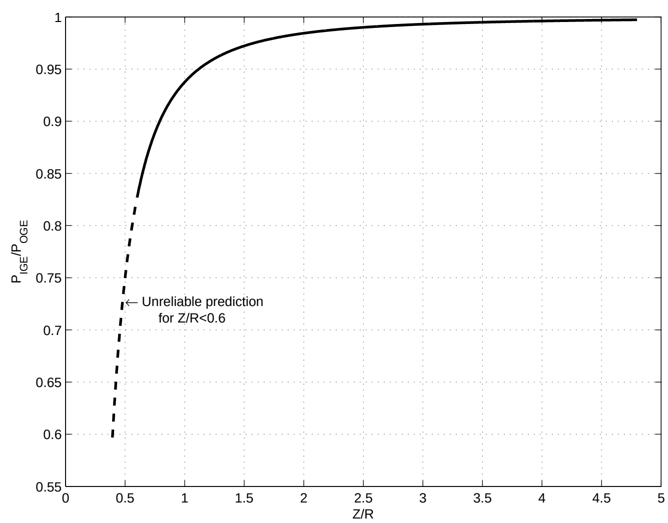

Figure 4–3: Variation of power in ground effect for constant thrust by Cheeseman

4.2 Experimental Results

An experiment using the X4-P single rotor was done to measure the effect of proximity to the ground on the produced thrust. The rotor was mounted on our test-stand and placed close to a wall (see Fig. 4–4), which represented the ground. Thrust and torque were measured while the rotor was rotating at a constant speed, at a given distance from the wall (henceforth referred as height above the ground). This procedure was repeated for various distances at three different constant rotational speeds, ranging from approximately

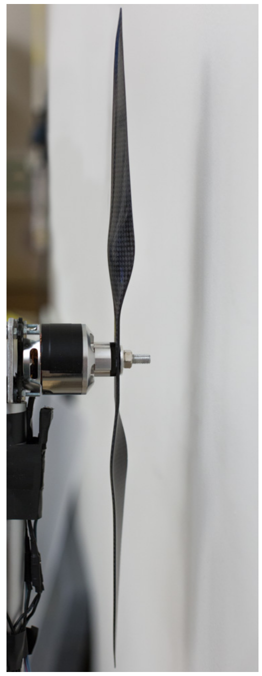

Figure 4–4: Ground effect fixture

2500 to 3000 RPM. Power values were then calculated by multiplying the torque by the rotational speeds (in rad/sec).

Linear interpolation was required in order to evaluate the thrust at constant power, for each height above the ground. For that, we first plotted the calculated power values (where $P = Q\Omega$) as a function of the thrust, producing a curve for each distance location, shown in Fig. 4–5. A value of constant power was selected[1] ($P_{const} = 20.84$W in the graph) and linear interpolation was used to determine the corresponding thrust for that power consumption, at that distance z. Note that, for the selected constant power, one

[1] It is noted that the choice of P_{const} will affect the results, but not significantly.

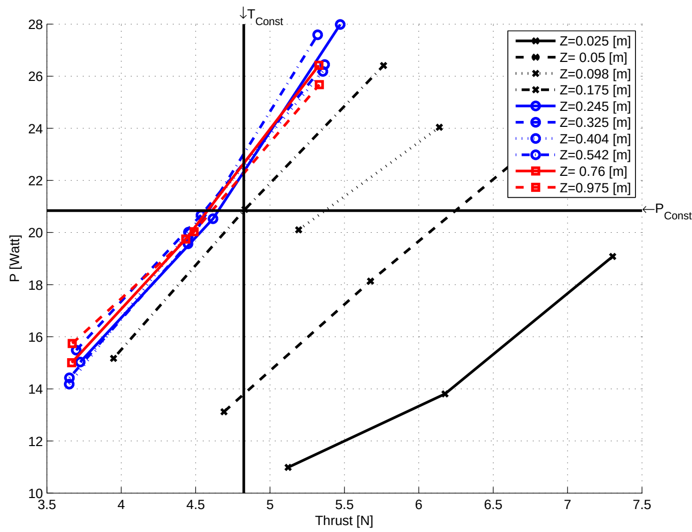

Figure 4–5: Variation of power vs. thrust for various heights above the ground

thrust value had to be linearly extrapolated for $Z = 0.025$m. Also note that, going from $Z = 0.975$m to $Z = 0.025$m along the line $P_{const} = 20.84$W corresponds to an increase of rotor speed from 2779 to 3073 RPM.

Using the interpolated data, a non-dimensional relation between thrust and height above the ground ratio (i.e. Z/R) for constant power was calculated, shown in Fig. 4–6. This plot also includes various ground effect measurements of other rotors, collected by Leishman[1].

We can see that the ground effect increases rapidly with decreasing distance from the ground. The measured values with constant power show similar behaviour to Cheeseman's model although Cheeseman's model rises more quickly as you come closer to the ground. Moreover, Cheeseman's model shows much higher ground effect in close proximity to the ground. However, as stated by Cheeseman, the ground effect prediction does not agree with measurements for values of Z/R smaller than 0.6. In addition, we can see

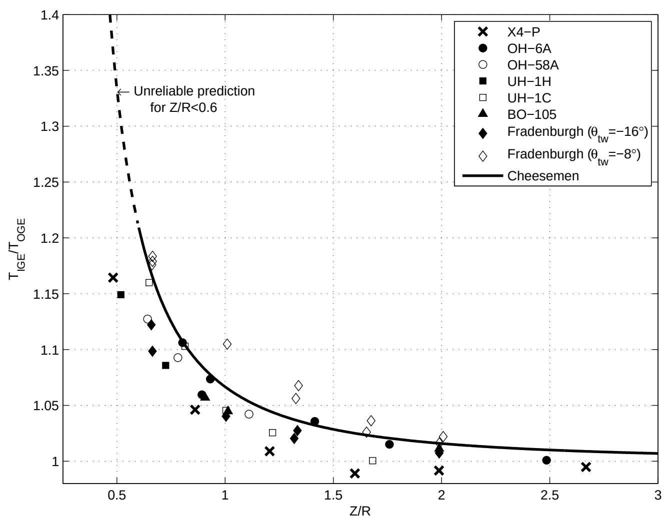

Figure 4–6: Variation of thrust in ground effect for constant power. Data from Leishman[1]

that the ground effect for constant power of the X4-P agrees very well with the other experimental measurements, especially those of the UH-1U rotor, which is the only rotor with measurements around $Z/R = 0.5$.

In practice, when operating a small UAV, rotational speeds commands are used to drive the motors. Hence, we show in Fig. 4–7 how the ground effect behaves for constant rotational speed. We can see that at very close proximity, the measured ground effect at constant speed is smaller compared to measurements with constant power and to Cheeseman's prediction. However, this close proximity is not crucial since the propeller at touchdown height (distance between upper rotors and landing gear) of the X8 UAV is approximately 300mm, which corresponds to a value of $Z/R \approx 1.5$, where measurements of T_{IGE}/T_{OGE} at constant speed agree very well with Cheeseman's prediction.

In order to determine the effect of propeller speed on the ground effect, we plotted the thrust ratio, T_{IGE}/T_{OGE}, vs. height above the ground ratio, Z/R, for the three constant

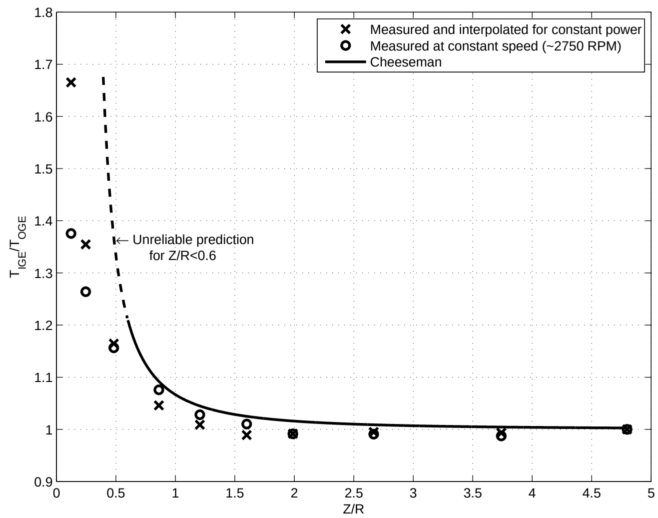

Figure 4–7: Variation of thrust in ground effect, comparing constant power and constant speed, with the X4-P rotor

rotational speeds, as shown in Fig. 4–8. The variation in speed does not have much im-

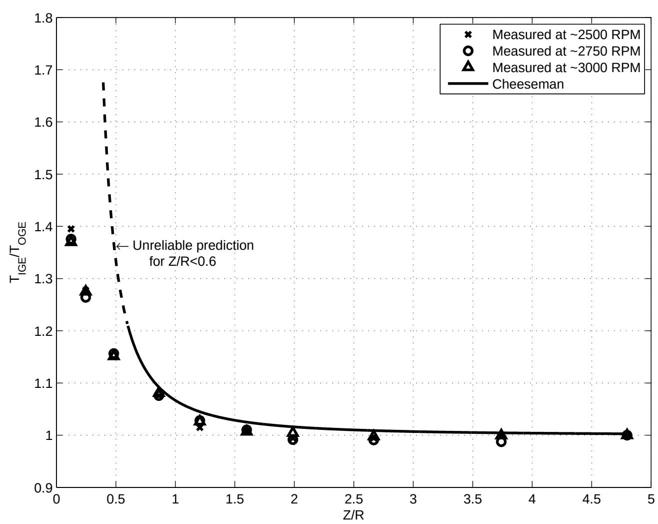

Figure 4–8: Variation of thrust in ground effect for various constant speeds, with the X4-P rotor

pact on the ground effect. This supports the premise that Cheeseman's model, although designed for constant power, can be used for predicting thrust in ground effect for the case of constant speed, for $Z/R > 0.6$ (based on Fig. 4–7).

As mentioned before, another way to consider the effect of proximity to the ground, is to evaluate the reduction in power required for producing constant thrust with variation of Z/R.

Once again linear interpolation was required in order to evaluate the power at constant thrust, for each height above the ground. Using Fig. 4–5, a value of constant thrust was selected[2] ($T_{const} = 4.82$N in the graph) and linear interpolation was used to determine the corresponding power consumption for that constant thrust, at that distance Z. Note that for the selected constant thrust, two points are required to be extrapolated at $Z = 0.025$m and $Z = 0.098$m. Note also that, going from $Z = 0.975$m to $Z = 0.025$m, the line $T_{const} = 4.82$N corresponds to a reduction of rotor speed from 2842 to 2441 RPM.

Using the interpolated data, a relation between power ratio, P_{IGE}/P_{OGE}, and height above the ground ratio, Z/R, for constant thrust was calculated, shown in Fig. 4–9. This plot also includes various ground effect measurements of other rotors, collected by Gilad[2]. We can see that the prediction for power reduction from eq. 4.2 agrees well with the measurements. As noted by Leishman[1], Cheeseman's model shows up to 25% reduction in power (for $Z/R = 0.5$). It can also be noted that, according to the measurements, the power reduction can reach up to approximately 50% in very close proximity to the ground. This agrees well with the results collected by Gilad[2], shown in Fig. 4–9.

[2] It is noted that the choice of T_{const} will affect the results, but not significantly.

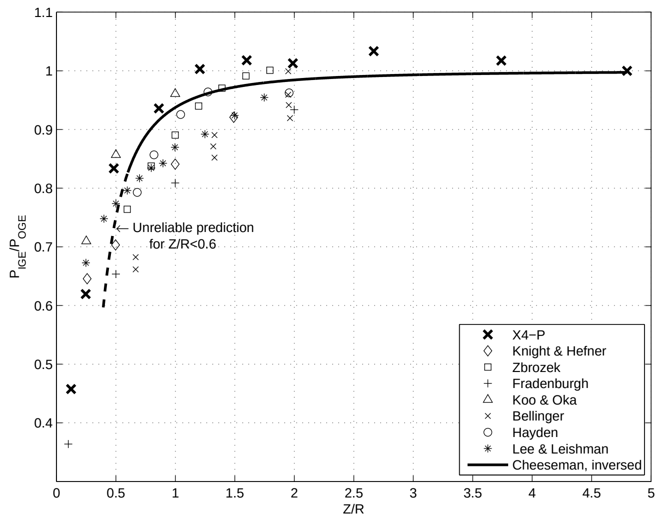

Figure 4–9: Variation of power reduction in ground effect for constant thrust. Data from Gilad[2]

Unfortunately, the strong ground effect is not feasible for the X8, since, as stated before, its construction does not permit such close proximity to the ground. However, even though the measurements in this study do not show any significant increase in thrust above $Z/R = 1.5$, it is possible that the quad-rotor configuration of the X8 will result in a stronger ground effect than compared to a single rotor. This was discussed by Griffiths[40] who noted that dual-rotor system was more affected by the ground, compared to single rotor, when operating in ground effect. The flow in this dual-rotor interference in ground effect was referred to as the ”fountain effect”, which became stronger as the dual-rotor system was approaching the ground. Moreover, this has also been empirically shown by Sharf[36] who performed in-flight measurements of the X8 UAV in ground effect for the hover case. It was noticed that the X8 coaxial-rotor in quad-rotor arrangement experienced higher ground effect than predicted by Cheeseman's model for $0.6 < Z/R < 3.0$.

Chapter 5
Conclusions

This study focused on developing and validating a physics-based blade element momentum theory model that allows prediction of thrust and torque of single and coaxial-rotors. This model was developed to be used in the simulation of the Draganflyer X8 UAV. The effect of proximity to the ground was also experimentally studied for a single rotor and compared to Cheeseman's ground effect model.

In this chapter we will summarize the major conclusions obtained during the work of this study.

5.1 Major Conclusions

1. The BEMT developed model was shown to reasonably predict the thrust and torque of both single and coaxial-rotors. However, the accuracy of the prediction is strongly affected by the assumed geometric and aerodynamic characteristics of the rotor, especially the zero-lift angle. Thus, particular care must be taken to obtain and use accurate data for these characteristics.
2. Considering swirl flow and removing the small angle assumption in the BEMT model did not prove to have a significant effect on the accuracy of model prediction. This supports the common use of the assumptions of no swirl and small angles in BEMT models.
3. For the hover case of the rotors mentioned in this thesis, stall did not have a noticeable effect on the performance.

4. Replacing the X8 UAV's rotors with the more conventional APC16x5.5MR rotors could be beneficial. The efficiency of the APC16x5.5MR rotor was shown to be better than the X8, and costs significantly less than the X8 rotor.
5. Cheeseman's model, although simple, can be used to predict the ground effect for constant thrust and power. In addition, it predicts the ground effect for constant speed, for $Z/R > 0.6$.

5.2 Limitations and Recommendations for Future Work

During this study some issues were raised regarding the test-stand, the estimated aerodynamic characteristics, rotor alternatives and the ground effect. These issues should be addressed in future work.

5.2.1 Test-stand

Axis alignment

In our two test-stands (for single and coaxial-rotors), it was quite difficult to align the propeller axis with the axis of the force/torque sensor's reference frame. A new test-stand has already been designed and should be constructed to ensure that the axis are aligned, without the need to readjust the alignment each time the test-stand is assembled.

Force/torque measurements noise

The force/torque measurements, captured by the ATI Gamma sensor, are noisy for all six axes. In the current work, an averaging filter was used to minimize the effect of the noise.

However, for the T_x axis, which is used to measure the torque values (as discussed in section 2.4.1), the resolution of the ATI Gamma sensor was not adequate due to the small torque values measured in our experiments. For that, a more sensitive sensor with higher resolution should be used to produce more reliable measurements.

Additional force/torque sensor for the coaxial-rotor

With the current coaxial-rotor test-stand, it is possible to measure only the total thrust and net torque of the thruster instead of the thrust and torque contributions of each rotor separately. This drawback makes it difficult to analyze the detailed behaviour of the coaxial-rotor and does not allow us realizing the total torque required to operate the rotors. It also eliminates the ability to validate the predicted thrust and torque of the BEMT model for the coaxial-rotor for each of the two rotors. This can be solved by mounting each rotor onto a separate force/torque sensor, which means we will have two sets of thrust and torque measurements, one for each rotor.

Captured data amalgamation

In our two current test-stands (for single and coaxial-rotors) the force/torque and rotational speed measurements are captured separately by two different softwares. This separation results in two issues, asynchronous data and extra work to combine the data to have both force/torque and rotational speed data in the same file. A redesign of the micro-controller which is used to command the ESCs is required in order to allow the rotational speed data to be captured synchronously with the force/torque data.

5.2.2 Aerodynamic characteristics

We showed that reasonable thrust simulation results were achieved using the selected method for obtaining the zero-lift angle, using the XFOIL software. However, considering the large thrust error this method can potentially cause, a better approach should be perused to obtain the zero-lift angle in order to decrease this potential error. The most trusted method of determining the zero-lift angle is to use wind tunnel measurements of lift vs. angle of attack. Unfortunately, this method has its own complexities that might not justify the improved accuracy over the use of XFOIL for obtaining zero-lift angle.

5.2.3 Rotor alternative

As discussed in section 3.4, our measurements of the thrust vs. torque showed improved efficiency of the APC16x5.5MR rotor compared to both Draganfly rotors. However, it would be more conclusive to experimentally compare the efficiency of the APC and Draganfly rotors by measuring the duration while hovering the X8 UAV with each rotor until the battery drains. If results show a significant advantage of the APC16x5.5MR rotor over the two Draganfly rotors, discuss with Draganfly Innovations Inc. the possibility of replacing the rotors with the better performing APC16x5.5MR, while maintaining the warranty.

5.2.4 Ground effect

When the experimental results of the ground effects for constant power and thrust were plotted in section 4.2, a few points had to be extrapolated to achieve continuous curves. In order to avoid extrapolation, one might want to take measurements at a wider range of rotational speeds (both lower and higher), for those measurements that are closest to the ground plane. As well, it might be worthwhile to take measurements at more than three speeds at each distance in order to reduce the error due to interpolation.

In addition, our test and model of the ground effect was performed for a single rotor while the UAV under discussion operates with a quad-rotor configuration. The ground effect should therefore be modeled and tested in the quad-rotor configuration. The model could try to adopt Cheeseman's model or perhaps use the free-vortex model of Griffiths and Leishman[40].

5.2.5 BEMT model for quad rotor

The BEMT model should be further validated to predict the thrust produced in a quad-rotor configuration, assuming the inter-rotor interference can be neglected since the wake contracts below the rotor disk[41]. In other words, the BEMT model should treat each rotor as a single rotor and predict its thrust. The thrusts of all four rotors should be summed to calculate the total thrust produced in the quad-rotor configuration. It should be noted that experimental results for a micro quad-rotor[41] (with rotor spacing of $0.3R$, similar to the X8) have shown a reduction of up to 6-7% in total thrust compared to four single rotors, however, this was observed mainly at high rotational speeds (higher than 12000 RPM). Then, experimental data of thrust vs. rotational speeds for a quad-rotor should be obtained, either using in-flight measurements or by building a custom-made test-stand, in order to compare and validate the simulation of the BEMT model.

REFERENCES

[1] J. Gordon Leishman. *Principal of Helicopter Aerodynamics*. Cambridge University Press, College Park, Maryland, 20742, USA, 2005.

[2] Mor Gilad, Inderjit Chopra, & Omri Rand. Performance Evaluation of a Flexible Rotor in Extreme Ground Effect. *37th European Rotorcraft Forum, Milan, Italy*, 2011.

[3] J. Gordon Leishman and Shreyas Ananthan. Aerodynamic Optimization of a Coaxial Proprotor. *Annual Forum Proceedings - AHS International*, I:64–86, 2006.

[4] Stephen D. Prior and Jonathon C. Bell. Empirical Measurements of Small Unmanned Aerial Vehicle Co-Axial Rotor Systems. *Journal of Science and Innovation*, 1(1):1–18, 2011.

[5] William John Macquorn Rankine. On the Mechanical Principles of the Action of Propellers. *Transactions of the Institute of of Naval Architects*, pages 13–39, 1865.

[6] W. Froude. On the Elementary Relation Between Pitch, Slip and Propulsive Efficiency. *Transactions Institute of Naval Architects*, 19:47–57, 1878.

[7] R. E. Froude. On the Part Played in Propulsion by Differences of Fluid Pressure. *Institute of Naval Architects*, 30:390, 1889.

[8] Glauert H. *Airplane Propellers*. Julius Springer, 1935.

[9] Stephane Drzewiecki. *Bulletin de L'Association Technique Maritime*, 1892.

[10] Stephane Drzewiecki. *Théorie générale de l'hélice: hélices aériennes et hélices marines*. Gauthier-Villars et cie., 1920.

[11] F.B. Gustafson and A. Gessow. *Effect of Rotor-tip Speed on Helicopter Hovering Performance and Maximum Forward Speed*. Wartime Reports. National Advisory Committee for Aeronautics, 1946.

[12] Alfred Gessow. Effect of Rotor-Blade Twist and Plan-Fonn Taper on Helicopter Hovering Performance. Technical Report NACA TN 1542, NACA, 1948.

[13] Lock C. N. H. and Yeatman D. Tables f'or Use in an Improved Method of' Airscrew Strip Theory Calculation. Technical Report 1674, Aeronautical Research Cimmittee Reoprts and Memoranda, October 1934.

[14] Robert D. Harrington. Full-Scale-Tunnerl Investigation of the Static-Thrust Performance of a Coaxial Helicopter Rotors. Technical Report Technical Note 2318, National Advisory Committee for Aeronautics, March 1951.

[15] R. C. Dingledein. Wind-Tunnel Studies of the Performance of Multirotor Configurations. Technical Report TN-3236, NACA, August 1954.

[16] Colin P. Coleman. A Survey of Theoretical and Experimental Coaxial Rotor Aerodynamic Research. Technical Report 3675, NASA, March 1997.

[17] Ashish Bagai and J. Gordon Leishman. Free-Wake Analysis of Tandem, Tilt-Rotor and Coaxial Rotor Configurations. *Journal of the American Helicopter Society*, 41(3):196–207, July 1996.

[18] J. Gordon Leishman and Shreyas Ananthan. An Optimum Coaxial Rotor System for Axial Flight. *Journal of the American Helicopter Society*, 53(4):366–381, October 2008.

[19] J. Gordon Leishman and Monica Syal. Figure of Merit Definition for Coaxial Rotors. *Journal of the American Helicopter Society*, 53(3):290–300, July 2008.

[20] J. Gordon Leishman. Aerodynamic Performance Considerations in the Design of a Coaxial Proprotor. *Journal of the American Helicopter Society*, 54(1):12005, January 2009.

[21] Jessica Yana and Omri Rand. Performance Analysis of a Coaxial Rotor System in Hover: Three Points of View. *International Conbgress of the Aeronautical Sciences*, (ICAS 2012-2.7.4), September 2012.

[22] Monica Syal. Contributions to the Aerodynamic Optimization of a Coaxial Rotor System. Masters of science, University of Maryland, 2012.

[23] Vinod K. Lakshminarayan and James D. Baeder. Computational Investigation of Small Scale Coaxial Rotor Aerodynamics in Hover. *47th AIAA Aerospace Sciences*

Meeting Including The New Horizons Forum and Aerospace Exposition, January 2009.

[24] Albert Betz. Schraubenpropeller mit geringstem Energieverlust. Mit einem Zusatz von l. Prandtl. *Nachrichten von der Gesellschaft der Wissenschaften zu Göttingen, Mathematisch-Physikalische Klasse*, 1919:193–217, 1919.

[25] Conor Stahlhut and J. Gordon Leishman. Aerodynamic Design Optimization of Proprotors for Convertible-Rotor Concepts. 2012.

[26] GNU General Public License.

[27] Barnes Warnock McCormick. *Aerodynamics, Aeronautics, and Flight Mechanics*. 1979.

[28] M. Drela. XFOIL: An Analysis and Design System for Low Reynolds Number Airfoils. In *Conference on Low Reynolds Number Airfoil Aerodynamics*. University of Notre Dame, 1989.

[29] Drela, M. and Youngren, H. Xfoil 6.9 user primer.

[30] Xavier Mauclère. Automatic 2D Airfoil Generation, Evaluation and Optimisation using MATLAB and XFOIL. Master's thesis, Technical University of Denemark, 2009.

[31] James G. Coder and Mark D. Maughmer. Comparisons of Theoretical Methods for Predicting Airfoil Aerodynamic Characteristics. *JOURNAL OF AIRCRAFT*, 51(No. 1), February 2014.

[32] Warren F. Phillips. *Mechanics of Flight*. Wiley, 2009.

[33] Ira H. Abbot and Albert E. Von Doenhoff. *Flight of Wing Sections*. 1959.

[34] Andy P. Broeren Michael S. Selig, James J. Guglielmo and Philippe Giguere. Summary of Low-Speed Airfoil Data, 1995.

[35] Bailey F. J. Jr. A Simplified Theoretical Method of Determining the Characteristics of a Lifting Rotor in Forward Flight. 1941.

[36] I. Sharf, M. Nahon, A. Harmat, W. Khan, M. Michini, N. Speal, M. Trentini, T. Tsadok and T. Wang. Ground Effect Experiments and Model Validation with Draganflyer X8 Rotorcraft. In *International Conference on Unmanned Aircraft Systems (ICUAS)*, 2014.

[37] H. G. Küssner. Helicopter Problems. Technical Memorandums No. 827, National Advisory Committee for Aeronautics, January 1937.

[38] A. Betz. The Ground Effect on Lifting Propellers. Technical Memorandums No. 836, National Advisory Committee for Aeronautics, April 1937.

[39] I. C. Cheeseman and W. E. Bennett. The Effect of the Ground on a Helicopter Rotor in Forward Flight. Technical report, Aeronautical research council reports and memoranda, 1957.

[40] Daniel A. Griffiths and J. Gor. A Study of Dual-Rotor Interference and Ground Effect Using a Free-Vortex Wake Model. *Circulation*, 2:1, 2002.

[41] Aaron M. Harrington. Optimal Propulsion System Design for a Micro Quad Rotor. Master's thesis, University of Maryland, 2011.

APPENDIX A

Aerodynamic characteristics of APC10x4.7SF propeller are given by,

$$C(y) = -115.810y^4 + 12.939y^3 - 4.580y^2 + 0.637y + 0.005 \tag{5.1}$$

$$\theta(y) = 333992.484y^5 - 139419.126y^4 + 22330.369y^3 - 1683.831y^2 + 54.709y - 0.192 \tag{5.2}$$

$$\alpha_0(y) = -13558.207y^4 + 3981.255y^3 - 416.279y^2 + 18.268y - 0.240 \tag{5.3}$$

$$C_d(\alpha') = 0.0013\alpha'^2 - 0.0031\alpha' + 0.0340 \tag{5.4}$$

and plotted in Fig. 5–1.

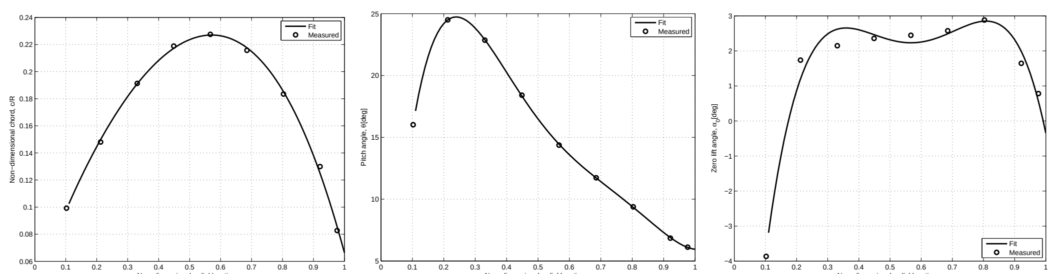

(a) Chord (b) Pitch angle (c) Zero-lift angle

Figure 5–1: APC10x4.7SF aerodynamic and geometrical properties

Aerodynamic characteristics of APC14x4.7SF propeller are given by,

$$C(y) = -138.466y^4 + 44.313y^3 - 8.400y^2 + 0.921y + 0.002 \tag{5.5}$$

$$\theta(y) = -1378241.212y^6 + 878076.370y^5 - 222973.529y^4 \tag{5.6}$$
$$+ 28595.046y^3 - 1912.360y^2 + 58.611y - 0.228$$

$$\alpha_0(y) = 13953.983y^5 - 8773.455y^4 + 2127.537y^3 \tag{5.7}$$
$$- 248.224y^2 + 13.874y - 0.257$$

$$C_d(\alpha') = 0.0010\alpha'^2 - 0.0058\alpha' + 0.0290 \tag{5.8}$$

and plotted in Fig. 5–2.

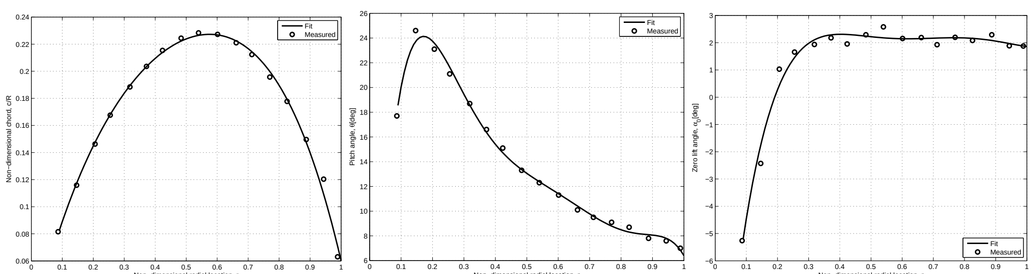

(a) Chord (b) Pitch angle (c) Zero-lift angle

Figure 5–2: APC14x4.7SF aerodynamic and geometrical properties

Aerodynamic characteristics of APC16x5.5MR propeller are given by,

$$C(y) = -1388.544y^5 + 631.229y^4 - 82.3764y^3 - 1.6734y^2 + 0.824y + 0.005 \tag{5.9}$$

$$\begin{aligned}\theta(y) = &-1294605.315y^6 + 960557.330y^5 - 284224.952y^4 + 42477.200y^3 \\ &- 3315.354y^2 + 121.489y - 1.142\end{aligned} \tag{5.10}$$

$$\begin{aligned}\alpha_0(y) = &-225995.392y^6 + 175217.274y^5 - 52820.121y^4 + 7806.501y^3 \\ &- 586.419y^2 + 20.651y - 0.204\end{aligned} \tag{5.11}$$

$$C_d(\alpha) = 0.001\alpha'^2 - 0.005\alpha' + 0.023 \tag{5.12}$$

and plotted in Fig. 5–3.

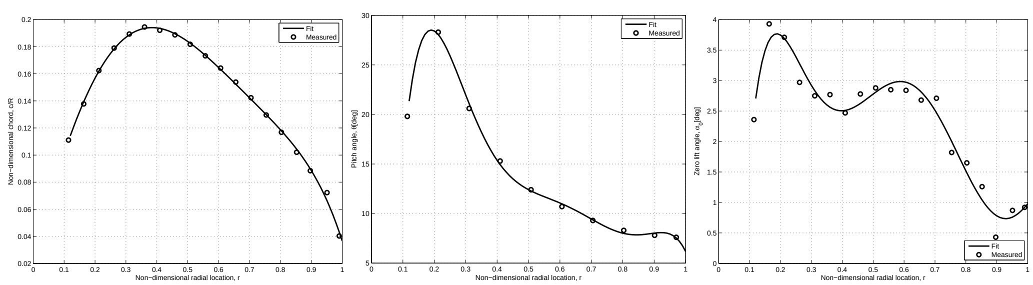

(a) Chord (b) Pitch angle (c) Zero-lift angle

Figure 5–3: APC16x5.5MR aerodynamic and geometrical properties

Aerodynamic characteristics of X4-P propeller are given by,

$$C(y) = -205.598y^4 + 98.949y^3 - 18.900y^2 + 1.586y - 0.017 \tag{5.13}$$

$$\theta(y) = -835595.597y^6 + 657206.264y^5 - 212511.153y^4 + 35915.331y^3 - 3303.686y^2 + 152.248y - 2.337 \tag{5.14}$$

$$\alpha_0(y) = 43450.930y^6 - 45431.750y^5 + 16865.147y^4 - 2927.654y^3 + 248.255y^2 - 9.229y + 0.121 \tag{5.15}$$

$$C_d(\alpha) = 0.0011\alpha'^2 - 0.0039\alpha' + 0.0208 \tag{5.16}$$

and plotted in Fig. 5–4.

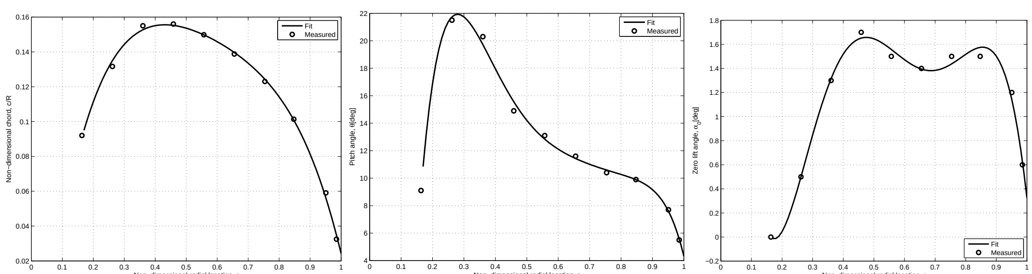

(a) Chord (b) Pitch angle (c) Zero-lift angle

Figure 5–4: X4-P aerodynamic and geometrical properties

Aerodynamic characteristics of X8 propeller are given by,

$$C(y) = -86667.231y^6 + 62241.97y^5 - 17962.877y^4 + 2656.391y^3 \tag{5.17}$$
$$- 211.255y^2 + 8.251y - 0.069$$
$$\theta(y) = -4484.586y^5 + 4772.198y^4 - 1744.842y^3 + 294.662y^2 \tag{5.18}$$
$$- 25.217y + 1.152$$
$$\alpha_0(y) = -9143.976y^5 + 4939.623y^4 - 1015.977y^3 + 96.305y^2 \tag{5.19}$$
$$- 3.948y + 0.062$$
$$C_d(\alpha) = 0.0010\alpha'^2 - 0.0028\alpha' + 0.0196 \tag{5.20}$$

and plotted in Fig. 5–5.

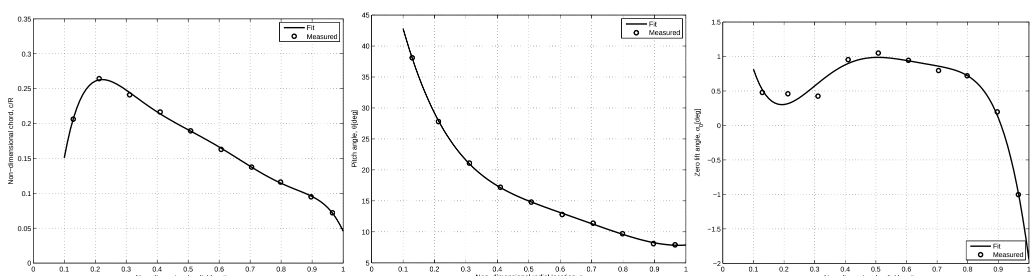

(a) Chord (b) Pitch angle (c) Zero-lift angle

Figure 5–5: X8 aerodynamic and geometrical properties